6-1-2022

TOI-1696: A Nearby M4 Dwarf With A 3 $R_\oplus$ Planet In The Neptunian Desert

M. Mori

J. H. Livingston

J. de Leon

See next page for additional authors

Recommended Citation

M. Mori et al. (2022). "TOI-1696: A Nearby M4 Dwarf With A 3 $R_\oplus$ Planet In The Neptunian Desert". *The Astronomical Journal*. Volume 163, Issue 6. DOI: 10.3847/1538-3881/ac6bf8
https://works.swarthmore.edu/fac-physics/491

The Astronomical Journal, 163:298 (19pp), 2022 June https://doi.org/10.3847/1538-3881/ac6bf8

TOI-1696: A Nearby M4 Dwarf with a 3 $R_\oplus$ Planet in the Neptunian Desert

Mayuko Mori[1], John H. Livingston[1,2,3], Jerome de Leon[1], Norio Narita[2,4,5], Teruyuki Hirano[2,3,6], Akihiko Fukui[4,5], Karen A. Collins[7], Naho Fujita[8], Yasunori Hori[2,3], Hiroyuki Tako Ishikawa[2,3], Kiyoe Kawauchi[5,9], Keivan G. Stassun[10], Noriharu Watanabe[11], Steven Giacalone[12], Rebecca Gore[12], Ashley Schroeder[12], Courtney D. Dressing[13], Allyson Bieryla[7], Eric L. N. Jensen[14], Bob Massey[15], Avi Shporer[16], Masayuki Kuzuhara[2,3], David Charbonneau[7], David R. Ciardi[17], John P. Doty[18], Emma Esparza-Borges[5,9], Hiroki Harakawa[19], Klaus Hodapp[20], Masahiro Ikoma[3,6], Kai Ikuta[11], Keisuke Isogai[11,21], Jon M. Jenkins[22], Taiki Kagetani[11], Tadahiro Kimura[23], Takanori Kodama[4], Takayuki Kotani[2,3,6], Vigneshwaran Krishnamurthy[2,3], Tomoyuki Kudo[19], Seiya Kurita[23], Takashi Kurokawa[2,24], Nobuhiko Kusakabe[2,3], David W. Latham[7], Brian McLean[25], Felipe Murgas[5,9], Jun Nishikawa[2,3,6], Taku Nishiumi[2,6,11], Masashi Omiya[2,3], Hugh P. Osborn[16,26], Enric Palle[5,9], Hannu Parviainen[5,9], George R. Ricker[16], Sara Seager[16,27,28], Takuma Serizawa[3,24], Huan-Yu Teng[29], Yuka Terada[30,31], Joseph D. Twicken[22,32], Akitoshi Ueda[2,3,6], Roland Vanderspek[16], Sébastien Vievard[2,19], Joshua N. Winn[33], Yujie Zou[11], and Motohide Tamura[1,2,3]

[1] Department of Astronomy, Graduate School of Science, The University of Tokyo, 7-3-1 Hongo, Bunkyo, Tokyo 113-0033, Japan; mori@astron.s.u-tokyo.ac.jp
[2] Astrobiology Center, 2-21-1 Osawa, Mitaka, Tokyo 181-8588, Japan
[3] National Astronomical Observatory of Japan, 2-21-1 Osawa, Mitaka, Tokyo 181-8588, Japan
[4] Komaba Institute for Science, The University of Tokyo, 3-8-1 Komaba, Meguro, Tokyo 153-8902, Japan
[5] Instituto de Astrofísica de Canarias (IAC), E-38205 La Laguna, Tenerife, Spain
[6] Department of Astronomy, School of Science, The Graduate University for Advanced Studies (SOKENDAI), 2-21-1 Osawa, Mitaka, Tokyo, Japan
[7] Center for Astrophysics | Harvard & Smithsonian, 60 Garden Street, Cambridge, MA 02138, USA
[8] Department of Astronomy, Kyoto University, Kitashirakawa-Oiwake-cho, Sakyo-ku, Kyoto 606-8502, Japan
[9] Departamento de Astrofísica, Universidad de La Laguna (ULL), E-38206 La Laguna, Tenerife, Spain
[10] Department of Physics and Astronomy, Vanderbilt University, Nashville, TN 37235, USA
[11] Department of Multi-Disciplinary Sciences, Graduate School of Arts and Sciences, The University of Tokyo, 3-8-1 Komaba, Meguro, Tokyo 153-8902, Japan
[12] Department of Astronomy, University of California Berkeley, Berkeley, CA 94720, USA
[13] Department of Astronomy, The University of California, Berkeley, CA 94720, USA
[14] Department of Physics & Astronomy, Swarthmore College, Swarthmore, PA 19081, USA
[15] Villa '39 Observatory, Landers, CA 92285, USA
[16] Department of Physics and Kavli Institute for Astrophysics and Space Research, Massachusetts Institute of Technology, Cambridge, MA 02139, USA
[17] Caltech/IPAC-NASA Exoplanet Science Institute, 770 S. Wilson Avenue, Pasadena, CA 91106, USA
[18] Noqsi Aerospace Ltd., 15 Blanchard Avenue, Billerica, MA 01821, USA
[19] Subaru Telescope, 650 N. Aohoku Place, Hilo, HI 96720, USA
[20] University of Hawaii, Institute for Astronomy, 640 N. Aohoku Place, Hilo, HI 96720, USA
[21] Okayama Observatory, Kyoto University, 3037-5 Honjo, Kamogatacho, Asakuchi, Okayama 719-0232, Japan
[22] NASA Ames Research Center, Moffett Field, CA 94035, USA
[23] Department of Earth and Planetary Science, Graduate School of Science, The University of Tokyo, 7-3-1 Hongo, Bunkyo, Tokyo 113-0033, Japan
[24] Institute of Engineering, Tokyo University of Agriculture and Technology, 2-24-16, Naka-cho, Koganei, Tokyo, 184-8588, Japan
[25] Space Telescope Science Institute, 3700 San Martin Drive, Baltimore, MD, 21218, USA
[26] NCCR/Planet-S, Universität Bern, Gesellschaftsstrasse 6, 3012 Bern, Switzerland
[27] Department of Earth, Atmospheric, and Planetary Sciences, Massachusetts Institute of Technology, Cambridge, MA 02139, USA
[28] Department of Aeronautics and Astronautics, Massachusetts Institute of Technology, Cambridge, MA 02139, USA
[29] Department of Earth and Planetary Sciences, School of Science, Tokyo Institute of Technology, 2-12-1 Ookayama, Meguro-ku, Tokyo 152-8551, Japan
[30] Institute of Astronomy and Astrophysics, Academia Sinica, P.O. Box 23-141, Taipei 10617, Taiwan, R.O.C.
[31] Department of Astrophysics, National Taiwan University, Taipei 10617, Taiwan, R.O.C.
[32] SETI Institute, Mountain View, CA 94043, USA
[33] Department of Astrophysical Sciences, Princeton University, 4 Ivy Lane, Princeton, NJ 08544, USA
Received 2022 March 3; revised 2022 April 21; accepted 2022 April 28; published 2022 May 31

Abstract

We present the discovery and validation of a temperate sub-Neptune around the nearby mid-M dwarf TIC 470381900 (TOI-1696), with a radius of $3.09 \pm 0.11\,R_\oplus$ and an orbital period of 2.5 days, using a combination of Transiting Exoplanets Survey Satellite (TESS) and follow-up observations using ground-based telescopes. Joint analysis of multiband photometry from TESS, Multicolor Simultaneous Camera for studying Atmospheres of Transiting exoplanets (MuSCAT), MuSCAT3, Sinistro, and KeplerCam confirmed the transit signal to be achromatic as well as refined the orbital ephemeris. High-resolution imaging with Gemini/'Alopeke and high-resolution spectroscopy with the Subaru InfraRed Doppler (IRD) confirmed that there are no stellar companions or background sources to the star. The spectroscopic observations with IRD and Infrared Telescope Facility SpeX were used to determine the stellar parameters, and it was found that the host star is an M4 dwarf with an effective temperature of $T_{\rm eff} = 3185 \pm 76$ K and a metallicity of [Fe/H] = 0.336 ± 0.060 dex. The radial velocities

measured from IRD set a 2σ upper limit on the planetary mass to be 48.8 $M_{\oplus}$. The large radius ratio ($R_p/R_\star \sim 0.1$) and the relatively bright near-infrared magnitude ($J = 12.2$ mag) make this planet an attractive target for further follow-up observations. TOI-1696 b is one of the planets belonging to the Neptunian desert with the highest transmission spectroscopy metric discovered to date, making it an interesting candidate for atmospheric characterizations with JWST.

Unified Astronomy Thesaurus concepts: Exoplanet astronomy (486); Exoplanet detection methods (489); Exoplanet systems (484); Transit photometry (1709); Photometry (1234); Multi-color photometry (1077); High resolution spectroscopy (2096); Spectroscopy (1558); Observational astronomy (1145); Time series analysis (1916); Transits (1711)

1. Introduction

Exoplanet population statistics from the Kepler mission (Borucki et al. 2010) revealed that there is a dearth of planets around the size of Neptune (~3–4$R_{\oplus}$) with orbital periods less than 2–4 days. This has been referred to as the "Neptunian Desert" or "photoevaporation desert" or simply "evaporation desert" (Szabó & Kiss 2011; Mazeh et al. 2016; Lopez 2017). The scarcity of planets in this region of the parameter space can be explained by photoevaporation, that is, atmospheric mass loss due to high-energy irradiation from the host star (Owen & Wu 2017). The small number of planets that have so far been found in the desert (e.g., West et al. 2019; Jenkins et al. 2020) are believed to retain substantial atmospheres (or are still in the process of losing them), but the physical mechanisms are not well understood. Comparing planets that have lost their atmospheres with those that have retained their atmospheres will be useful to understand the processes such as photoevaporation theory. Therefore, it is important to increase the number of planets in this region and reveal the nature of their atmospheres. The Transiting Exoplanets Survey Satellite (TESS; Ricker et al. 2015), which has identified over 5000 exoplanet candidates so far[34] (NASA Exoplanet Science Institute 2020), made it possible to discover more planets in the Neptunian Desert.

In this paper, we report the validation of a new planet around the mid-M dwarf TOI-1696, whose transits were identified by the TESS mission. The planet TOI-1696 b has a sub-Neptune size ($3.09 \pm 0.11\ R_{\oplus}$) and an orbital period of 2.5 days, which places it within (or near the boundaries of) the Neptunian desert.

The large radius ratio ($R_p/R_\star \sim 0.1$) makes the planet's transits deep, and combined with the relatively bright near-infrared magnitude ($J = 12.2$ mag) of the star, the planet is one of the best targets for future atmospheric research via transmission spectroscopy.

The rest of this paper is organized as follows. In Section 2, we present the observational data and the reduction procedures used for the analysis. In Section 3, we explain the analysis methods and results. In Section 4, we discuss the features of the planet and its future observational prospects, concluding with a summary in Section 5.

2. Observations and Data Reduction

2.1. Transit Photometry—TESS

TESS observed TOI-1696 with a 2 minute cadence in Sector 19 from 2019 July 25 to August 22, resulting in photometry spanning approximately 27 days with a gap of about one day in the middle when the satellite reoriented itself for data downlink near perigee. Light curves were produced by the Science Processing Operations Center (SPOC) photometry pipeline (Jenkins 2002; Jenkins et al. 2010, 2016) using the aperture shown in Figure 1. We used the `PDCSAP` light curves produced by the SPOC pipeline (Stumpe et al. 2012; Smith et al. 2012; Stumpe et al. 2014) for our transit analyses. TOI-1696 is located in a fairly crowded field, owing to its low galactic latitude ($b = -0.^{\circ}81$). The SPOC pipeline applies a photometric dilution correction based on the `CROWDSAP` metric, which we independently confirmed by computing dilution values based on Gaia Data Release 2 (DR2) magnitudes.[35]

TOI-1696.01 was detected by the SPOC pipeline in a transiting planet search, and the candidate was subsequently reported to the community by the TESS Science Office (TSO) on 2020 January 30 via the TESS Object of Interest (TOI; Guerrero et al. 2021) Releases portal.[36] The candidate passed all data validation diagnostic tests (Twicken et al. 2018) performed by the SPOC.[37] The SPOC pipeline removed the transit signals of TOI-1696.01 from the light curve and performed a search for additional planet candidates (Li et al. 2019), but none were reported.

We independently confirmed the transit signal found by the SPOC. After removing stellar variability and residual instrumental systematics from the `PDCSAP` light curve using a second-order polynomial Savitzky–Golay filter with a window = 1001, we searched for periodic transit-like signals using the transit least-squares algorithm (TLS; Hippke & Heller 2019),[38] resulting in the detection of TOI-1696.01 with a signal detection efficiency (SDE) of 11.6, a transit signal-to-noise ratio (S/N) of 7.4, orbital period of 2.50031 ± 0.00001 days, and transit depth of 10.6 parts per thousand (ppt), which is consistent with the values reported by the TESS team on the Exoplanet Follow-up Observing Program for TESS (ExoFOP-TES;[39] ExoFOP 2019). We subtracted this signal and repeated the transit search, but no additional signals with SDE above 10 were found. TLS also reports the approximate depths of each individual transit; we note that these transit depths and uncertainties are useful for diagnostic purposes only, as they are simplistically determined from the mean and standard deviation of the in-transit flux. The depths of the odd transits are within 1.5σ of the even transits, suggesting a low probability of either signal being caused by an eclipsing binary at twice the detected period. The TLS detection is shown in Figure 2.

[34] As of 2022 February per https://exoplanetarchive.ipac.caltech.edu/.

[35] Approximating Gaia R_p as the TESS bandpass, and assuming a FWHM of 25″.

[36] https://tess.mit.edu/toi-releases/

[37] Full vetting report available for download at https://exo.mast.stsci.edu/exomast_planet.html?planet=TOI169601.

[38] https://transitleastsquares.readthedocs.io/en/latest/index.html

[39] https://exofop.ipac.caltech.edu/tess/

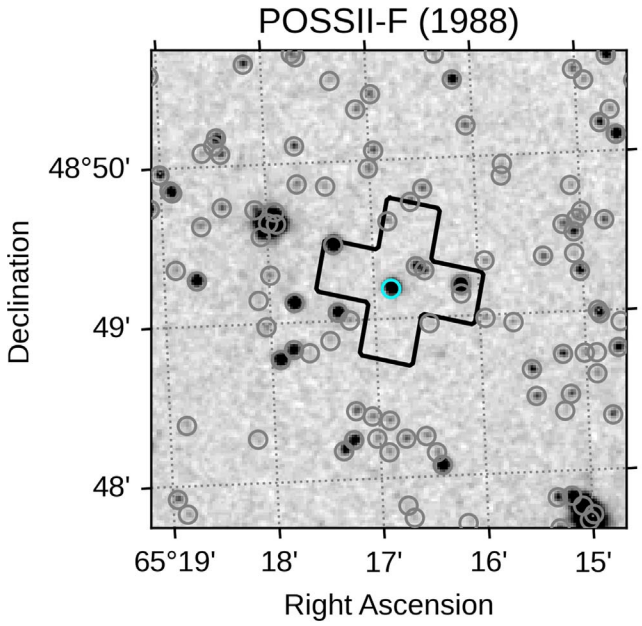

Figure 1. Archival imaging from POSSII-F survey (taken in 1998; Reid et al. 1991) with the TESS photometric aperture (black outline) and Gaia sources (gray circles). The cyan circle indicates the position of TOI-1696; we note the proper motion is low enough that its current position is not significantly offset in the archival image.

2.2. Transit Photometry—FLWO/KeplerCam

We used KeplerCam, mounted on the 1.2 m telescope located at the Fred Lawrence Whipple Observatory (FLWO) atop Mt. Hopkins, Arizona, to observe a full transit on 2020 February 17. KeplerCam has a $23\farcm1 \times 23\farcm1$ field of view and operates in binned by 2 mode producing a pixel scale of $0\farcs672$. Images were obtained in the i band with an exposure time of 300 s. A total of 29 images were collected over 144 minutes. The data were reduced using standard IDL routines, and photometry was performed using the `AstroImage`Jsoftware package (Collins et al. 2017). These data are shown in Figure 9.

2.3. Transit Photometry—LCO/SINISTRO

We observed a full transit on 2020 November 13, using Sinistro, an optical camera mounted on a 1 m telescope located at McDonald Observatory in Texas, operated by Las Cumbres Observatory (LCO; Brown et al. 2013). Sinistro has a $26\farcm5 \times 26\farcm5$ field of view with a pixel scale of $0\farcs389$. We observed 62 images in total during 339 minutes, using a V-band filter, with an exposure time of 5 minutes. The data were reduced by the standard `BANZAI` pipeline by the Las Cumbres Observatory Global Telescope (LCOGT; McCully et al. 2018), and photometry was performed using `AstroImage`Jsoftware. These data are shown in Figure 9.

2.4. Transit Photometry—LCO/MuSCAT3

Multicolor Simultaneous Camera for studying Atmospheres of Transiting exoplanets 3 (MuSCAT3) is a multiband simultaneous camera installed on the 2 m Faulkes Telescope North at LCO on Haleakala, Maui (Narita et al. 2020). It has four channels, enabling simultaneous photometry in the g (400–550 nm), r (550–700 nm), i (700–820 nm), and z_s (820–920 nm) bands. Each channel has a 2048×2048 pixel CCD camera with a pixel scale of $0\farcs27$, providing a $9\farcm1 \times 9\farcm1$ field of view. We observed a full transit of TOI-1696.01 on 2020 December 23, from BJD 2459206.703523 to 2459206.827246. We took 36, 41, 89, and 131 exposures with exposure times of 300, 265, 120, and 80 s in the g, r, i, and z_s bands, respectively.

The data reduction was conducted by the standard LCOGT `BANZAI` pipeline. Then differential photometry was conducted by a customized aperture-photometry pipeline for the MuSCAT series (Fukui et al. 2011). The optimized aperture radii are 8, 6, 10, and 8 pixels ($2\farcs16$, $1\farcs62$, $2\farcs7$, and $2\farcs16$) for the g, r, i, and z_s bands, respectively. We optimized a set of comparison stars for each band to minimize the dispersion of the light curves. For computational efficiency, and to achieve a more uniform S/N, we subsequently binned the g, r, i, and z_s data to 300, 240, 180, and 120 s, respectively. These data are shown in Figure 7.

2.5. Transit Photometry—NAOJ 188 cm/MuSCAT

We also observed a full transit with MuSCAT (Narita et al. 2015), which is installed on the 188 cm telescope of the National Astronomical Observatory of Japan (NAOJ) in Okayama, Japan. MuSCAT has a similar optical design as MuSCAT3 but has three CCD cameras for the g, r, and z_s bands. On the night of 2021 July 28 we observed TOI-1696 from BJD 2459424.228358 to 2459424.30679. At that point, the r-band camera was not available due to an instrumental issue, so we observed with only the g and z_s bands, using an exposure time of 60 s for both bands.

The data reduction and differential photometry was performed using the pipeline described in Fukui et al. (2011). The optimized aperture radii were 4 and 6 pixels ($1\farcs44$ and $2\farcs16$) for the g and z_s bands, respectively. Similarly to the MuSCAT3 data, we binned the g and z_s data to 300 and 120 s, respectively. These data are shown in Figure 8.

2.6. Speckle Imaging—Gemini/'Alopeke

On the nights of 2020 December 03 and 2021 October 14, TOI-1696 was observed with the 'Alopeke speckle imager (Scott 2019), mounted on the 8.1 m Gemini North telescope on Maunakea. 'Alopeke simultaneously acquires data in two bands centered at 562 nm and 832 nm using high-speed electron-multiplying CCDs (EMCCDs). We collected and reduced the data following the procedures described in Howell et al. (2011). The resulting reconstructed image achieved a contrast of $\Delta\mathrm{mag} = 5.8$ at a separation of $1''$ in the 832 nm band. No secondary sources were detected. The data taken on 2021 October 14 are shown in Figure 3.

2.7. Adaptive Optics Imaging—Palomar/PHARO

On 2021 September 19 we conducted near-infrared high-resolution imaging using the adaptive optics instrument Palomar High Angular Resolution Observer (PHARO) mounted on the 5 m Hale telescope at Palomar Observatory (Hayward et al. 2001). We observed TOI-1696 separately in the $Br\gamma$ (2.18 μm) and H_{cont} (2.29 μm) bands, reaching a contrast of $\Delta\mathrm{mag} = 8$ at a separation of $1''$ in both bands. The AO images and corresponding contrast curves are shown in Figure 4.

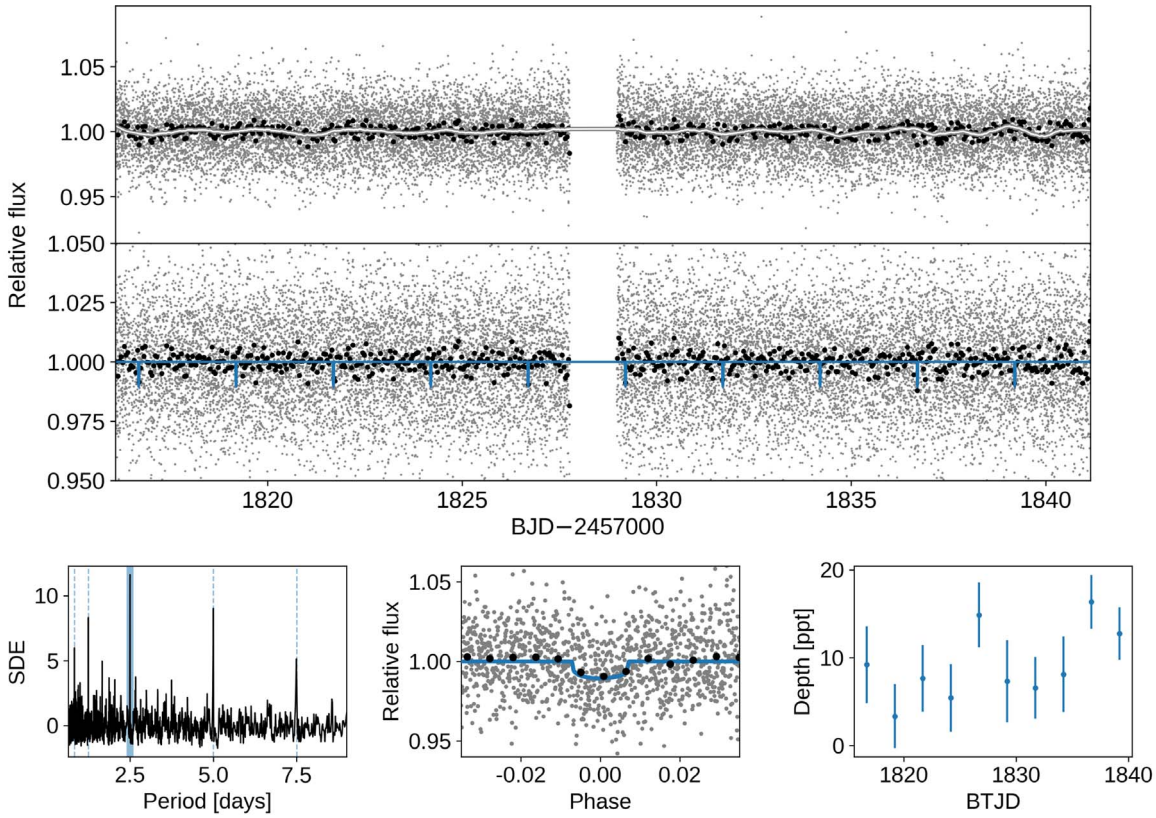

Figure 2. Upper panels show the TESS PDCSAP light curve with the Savitzky–Golay (window = 1001) variability model (top), and the flattened light curve with the TLS model (bottom). The lower panels show the TLS power spectrum (left), folded TESS light curve with the TLS model (middle), and individual transit depths from the TLS (right).

2.8. High-resolution Spectroscopy—Subaru/IRD

We obtained high-resolution spectra of TOI-1696 in the near-infrared with the InfraRed Doppler (IRD; Tamura et al. 2012; Kotani et al. 2018), mounted on the 8.2 m Subaru telescope. IRD can achieve a spectral resolution of ∼70,000 in the wavelength range 930 nm to 1740 nm. The derived spectra were used for three purposes: to search for spectral companions (e.g., double-lined spectroscopic binary scenarios), to measure fundamental stellar parameters (e.g., effective temperature and metallicity), and to rule out large radial velocity (RV) variations that would indicate an eclipsing binary (EB), as well as placing a limit on the mass of the planet. From UT 2021 January 30 to 2022 January 08, we obtained 13 spectra of TOI-1696 using 1800 s exposure times, as part of a Subaru Intensive Program (Proposal IDs S20B-088I and S21B-118I). The raw data were reduced using `IRAF` (Tody 1993) as well as a pipeline for the detector's bias processing and wavelength calibrations developed by the IRD instrument team (Kuzuhara et al. 2018; Hirano et al. 2020). For the RV analyses and stellar parameter derivation, we computed a high-S/N coadded spectrum of the target following the procedures described in Hirano et al. (2020).

For use as a spectral template in the analysis described in Section 3.2, we also downloaded archival IRD data of GJ 699 (Barnard's Star),[40] which were obtained on 2019 March 23 (HST). We reduced and calibrated the GJ 699 data following the same procedures as the TOI-1696 data.

[40] Using the Subaru–Mitaka–Okayama–KisoArchive (SMOKA).

2.9. Medium-resolution Spectroscopy—IRTF/SpeX

We collected observations of TOI-1696 on UT 2020 December 09 using SpeX, a medium-resolution spectrograph on the NASA Infrared Telescope Facility (IRTF) on Maunakea (Rayner et al. 2003). We obtained our observations in SXD mode with a $0\farcs3 \times 15''$ slit, providing a spectral resolution of $R \approx 2000$ over a wavelength range from 700 nm to 2550 nm. In order to remove the sky background and reduce systematics, the spectra were collected using an ABBA nod pattern (with a separation of $7\farcs5$ between the A and B positions) and with the slit synced to the parallactic angle. We reduced our spectra using the `Spextool` reduction pipeline (Cushing et al. 2004) and removed telluric contamination using `xtellcor` (Vacca et al. 2003). The derived spectra were used to calculate the stellar metallicity.

3. Analysis and Results

3.1. Stellar Parameter Estimation

In the next subsections we estimate the fundamental stellar parameters of TOI-1696. First, the stellar effective temperature $T_{\rm eff}$ and metallicity [Fe/H] are derived from two independent methods; one is from the IRD spectra, and the other is from the SpeX spectra and photometric relations. Second, the stellar radius $R_\star$, mass $M_\star$, and other related parameters are derived using empirical relations and the above $T_{\rm eff}$ and [Fe/H] values.

3.1.1. Estimation of T_{eff} and [Fe/H]: from IRD Spectra

We derived the effective temperature $T_{\rm eff}$ and abundances of individual elements [X/H] from the coadded IRD spectrum. To

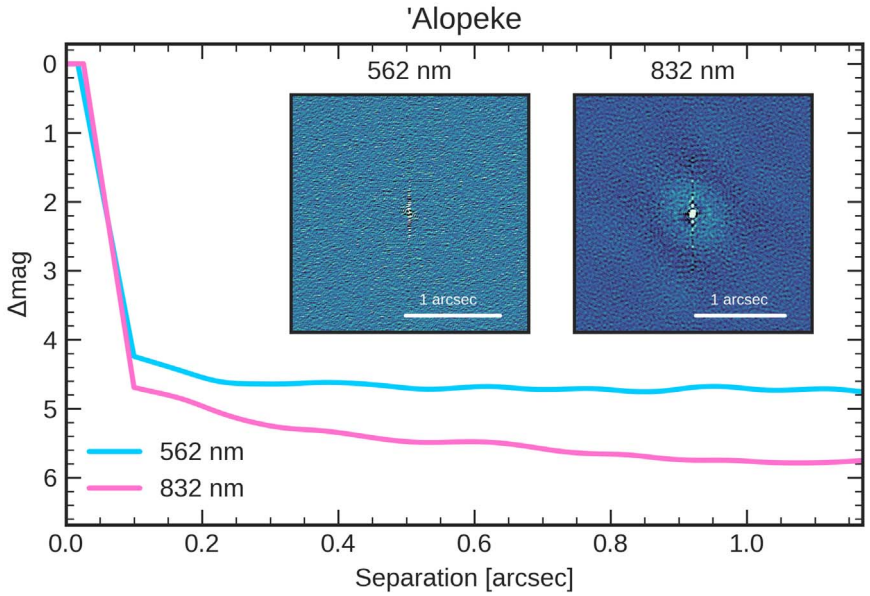

Figure 3. Gemini/'Alopeke reconstructed images and contrast curves produced as described in Section 2.6.

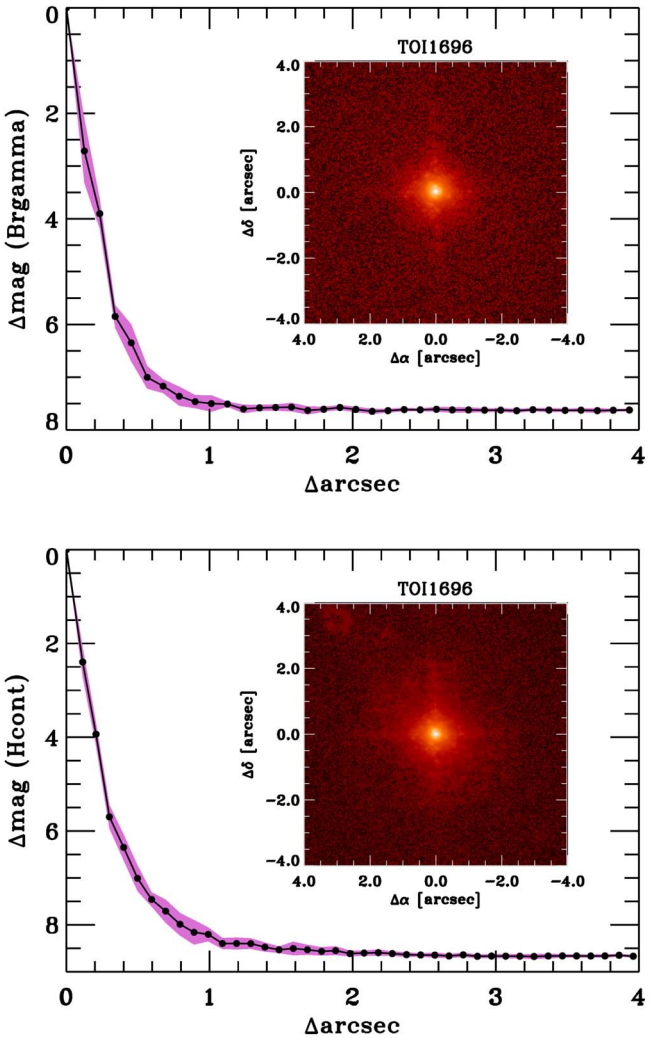

Figure 4. Palomar/PHARO images and contrast curves (top: Brγ; bottom: H_{cont}) produced as described in Section 2.7.

avoid amplifying noise in the spectrum, we decided not to deconvolve the instrumental profile prior to these analyses.

We determined the parameters by the equivalent width comparison of individual absorption lines between the synthetic spectra and the observed ones. For $T_{\rm eff}$ estimation, 47 FeH molecular lines in the Wing–Ford band at 990–1020 nm were used as in Ishikawa et al. (2022). We also derived the abundance of eight metal elements as described in Appendix A.1.

We iterated the $T_{\rm eff}$ estimation and the abundance analysis alternately until $T_{\rm eff}$ and metallicity were consistent with each other. First, we derived a provisional $T_{\rm eff}$ assuming the solar metallicity ([Fe/H] = 0), and then we determined the individual abundances of the eight elements [X/H] using this provisional $T_{\rm eff}$. Second, we redetermined $T_{\rm eff}$ adopting the iron abundance [Fe/H] as the input metallicity, and then we redetermined the abundances using the new $T_{\rm eff}$. We iterated the estimation of $T_{\rm eff}$ and [Fe/H] until the final results and the results of the previous step agreed within the error margin. As a result, we derived $T_{\rm eff} = 3156 \pm 119$K and [Fe/H] $= 0.333 \pm 0.088$ dex.

3.1.2. *Estimation of* T_{eff} *and [Fe/H]: from SpeX Spectra and Photometric Relations*

Before analyzing our SpeX spectra, we corrected the data to the lab reference frame using `tellrv`[41] (Newton et al. 2014, 2022). We then determined the metallicity with `metal`[42] (Mann et al. 2013), using only the *K*-band part of the spectrum, which is historically the most reliable, although the metallicities from the *H* and *J* bands are broadly consistent.

We calculated the stellar parameters using a series of photometric relations, following Section 4.3 of Dressing et al. (2019). First, we calculated the luminosity of the star using the Gaia Early Data Release 3 (EDR3) distance (Stassun & Torres 2021),

[41] https://github.com/ernewton/tellrv
[42] https://github.com/awmann/metal

Two Micron All Sky Survey (2MASS) J magnitude, r magnitude (from the Carlsberg Meridian Catalogue; Muiños & Evans 2014), and metallicity-dependent r–J bolometric correction in Table 3 of Mann et al. (2015). Next, we calculated the radius of the star using the relation between $R_\star$, the absolute K magnitude, and the [Fe/H] defined in Table 1 of Mann et al. (2015). Lastly, we calculated $T_{\rm eff}$ using the Stefan–Boltzmann law. As a result, we derived $T_{\rm eff} = 3207 \pm 99$K and [Fe/H] $= 0.338 \pm 0.083$ dex.

The strong agreement in $T_{\rm eff}$ and [Fe/H] between the two methods suggests a high degree of reliability of the measurements. For the following analyses, we used the weighted mean of the two respective measurements for $T_{\rm eff}$ and [Fe/H], specifically, $T_{\rm eff} = 3185 \pm 76$ K and [Fe/H] $= 0.336 \pm 0.060$ dex.

3.1.3. Estimation of Stellar Radius and Mass

We estimated other stellar parameters such as the stellar mass $M_\star$, radius $R_\star$, surface gravity $\log g$, mean density $\rho_\star$, and luminosity $L_\star$ following the procedure described in Hirano et al. (2021). In short, the distributions of the stellar parameters are derived from a Monte Carlo approach using a combination of several empirical relations as well as the observed and literature values.

The $R_\star$ value was calculated through the empirical relation from Mann et al. (2015) and $M_\star$ from Mann et al. (2019). In deriving the stellar parameters by Monte Carlo simulations, we adopted Gaussian distributions for $T_{\rm eff}$ and [Fe/H] based on our spectroscopic analyses (see Sections 3.1.1 and 3.1.2), the apparent K_s-band magnitude from 2MASS, and the parallax from Gaia EDR3 (Stassun & Torres 2021). We assumed zero extinction ($A_V = 0$), considering the proximity of the star to Earth.

As a result, we derived $R_\star = 0.2775 \pm 0.0080\,R_\odot$ and $M_\star = 0.255 \pm 0.0066\,M_\odot$ along with the other parameters listed in A1. By interpolating Table 5 of Pecaut & Mamajek (2013), we determined the spectral type of TOI-1696 to be M4V (M3.9V $\pm$ 0.2).

To check the robustness of this analysis, we confirmed them to be in good agreement with the stellar parameters derived through independent analyses based on SED fitting and `isochrones` (see Appendix A.2 and A.3).

3.2. Search for Spectroscopic Binary Stars

If a stellar companion orbits the target star, the observed spectra will generally be the combination of two stellar spectra with different radial velocities. To see if TOI-1696 is a double-lined spectroscopic binary, we calculated the cross-correlation function (CCF) of the TOI-1696's IRD spectra with that of the well-known single-star GJ 699 (Barnard's Star). The spectrum of TOI-1696 used for the analysis was obtained on UT 2021 January 30 08:53, which corresponds to an orbital phase of 0.247 based on the TESS ephemeris.

For the analysis, we divided the spectra into six wavelength bins that are less affected by telluric absorption: [988, 993 nm], [995, 1000 nm], [1009, 1014 nm], [1016, 1021 nm], [1023, 1028 nm], and [1030, 1033 nm]. We corrected the telluric absorption signal using the spectra of the rapid-rotator HIP 74625, which was observed on the same night. The CCF to the template spectrum was calculated for each segment, after barycentric velocity correction. Finally, we computed the median of the CCFs from each segment. As shown in Figure 5, the resulting CCF is clearly single-peaked. If the observed transit signals were actually caused by an eclipsing stellar companion, the RV difference at quadrature would be >100 km s^{-1}, which would result in a second peak in the CCF given that the flux of such a companion would be detectable. We thus conclude TOI-1696 is not an eclipsing binary.

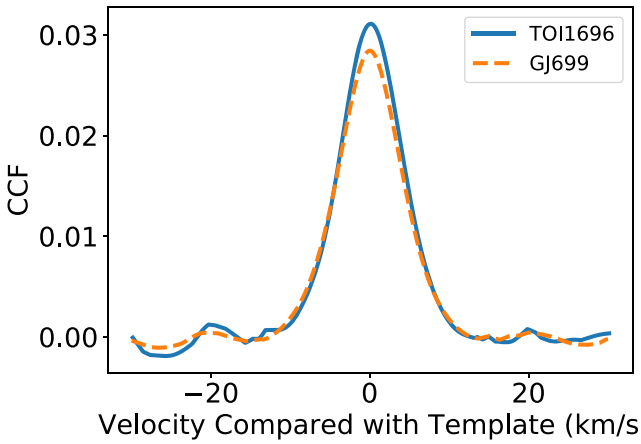

Figure 5. Calculated CCF of the IRD spectrum of TOI-1696 taken on 2021 January 30 at the orbital phase 0.247, to the template spectrum of GJ699, exhibiting a single peak with width 9.2 k m s^{-1}. The dashed line shows the autocorrelation function of the GJ699 spectrum as a reference.

3.3. Stellar Age

Because young stars are active and rapidly rotating, the stellar activity and rotation period can be used as proxy for determining its youth. We did not find any stellar rotational signal in the TESS SPOC light curve, suggesting that the star is not very active. Similarly, no strong rotational signal was found in archival photometric data from Zwicky Transient Facility (ZTF) Data Release 9 (Bellm et al. 2019; Masci et al. 2019) and the All Sky Automated Survey for SuperNovae (ASAS-SN; Kochanek et al. 2017).

GJ 699 has a rotation period of 145 days and $v \sin i$ of less than 3 km s^{-1} (Toledo-Padrón et al. 2019), which is below the limit of IRD's resolving power ($\sim$70000, corresponding to $\sim$4.5 km s^{-1}). While the CCF of TOI-1696 has an FWHM value consistent with that of GJ 699 (see Figure 5), even if we assume the rotation axis of TOI-1696 is in the plane of the sky, relatively short rotation periods cannot be ruled out, as their rotational broadening would not be resolvable with IRD. However, fast rotation would most likely be accompanied with surface magnetic activity levels that would produce detectable photometric signals. We also used `banyan` Σ (Gagné et al. 2018) to check if TOI-1696 is a member of any known stellar associations, using its proper motion and the parallax from Gaia EDR3. `banyan` Σ tool[43] returned a value of 99.9% field star, suggesting it is not a member of any nearby young moving group. The nondetection by Galaxy Evolution Explorer also means that the star is not young enough to be bright in the UV. We thus conclude that TOI-1696 is most likely a relatively old, slow rotator.

[43] http://www.exoplanetes.umontreal.ca/banyan/

3.4. Transit Analysis

We jointly fit the TESS, KeplerCam, Sinistro, MuSCAT3, and MuSCAT data sets using the `PyMC3`[44] (Salvatier et al. 2016), `exoplanet`[45] (Foreman-Mackey et al. 2019), `starry` (Luger et al. 2019), and `celerite2` (Foreman-Mackey et al. 2017; Foreman-Mackey 2018) software packages.

3.4.1. Mean Model

We assumed a linear ephemeris, a circular orbit, quadratic limb darkening, and a chromatic transit depth. The model was implemented using a Keplerian orbit (`exoplanet.orbits.KeplerianOrbit`) with eccentricity fixed to zero and a quadratically limb-darkened `starry` transit model (provided by `exoplanet.LimbDarkLightCurve`) with separate scaled planet radius ($R_P/R_\star$) parameters for each photometric bandpass. We sampled in the stellar mass and radius instead of the scaled semimajor axis ($a/R_\star$), taking advantage of the alternative parameterizations accepted by `exoplanet.orbits.KeplerianOrbit`. The full set of transit parameters defining the mean model was thus: the stellar mass $M_\star$, stellar radius $R_\star$, mid-transit time T_0, orbital period P, impact parameter b, planet-to-star radius ratio $R_P/R_\star$ (i), and quadratic limb darkening parameters u_1 (i) and u_2 (i), where i is the ith photometric bandpass from the transit data sets ($i \in \{T, V, g, r, i, z\}$).

3.4.2. Noise Model

To account for systematics in the ground-based data sets we included a linear model of airmass and other covariates, such as the pixel response function peak, width, and centroids, when available. To account for the stellar variability and residual systematics in the TESS `SPOC` light curve, we included a Gaussian process (GP; Rasmussen & Williams 2005) model with a Matérn-3/2 covariance function (as implemented in `celerite2.theano.terms.Matern32Term`). To account for the possibility of underestimated or overestimated measurement uncertainties, we included a white noise scale parameter for each data set/band, enabling the errors to be estimated simultaneously with other free parameters while retaining the relative weighting of data points within each data set.

3.4.3. Priors

We placed Gaussian priors on the white noise scale parameters, with the center and width equal to unity, and Gaussian priors on the stellar mass and radius based on the results in Table 1. We also placed Gaussian priors on the limb darkening coefficients based on interpolation of the parameters tabulated in Claret et al. (2012) and Claret (2017), propagating the uncertainties in the stellar parameters in Table 1 via Monte Carlo simulation.[46] We used uniform priors for all other free parameters, except for the GP hyperparameters (red noise amplitude and length scale), which we sampled in logarithmic space with wide (uninformative) Gaussian priors.

3.4.4. Exploration of Parameter Space

To optimize the model we used the gradient-based `BFGS` algorithm (Nocedal & Wright 2006) implemented in `scipy.optimize` to find the initial maximum a posteriori (MAP) parameter estimates. We then used these estimates to initialize an exploration of the parameter space via "no U-turn sampling" (NUTS; Hoffman & Gelman 2014), an efficient gradient-based Hamiltonian Monte Carlo (HMC) sampler implemented in `PyMC3`. We sampled four independent chains initialized with the MAP parameter values for 3000 tuning steps followed by an additional 1000 steps. The MAP solution found during sampling had a higher posterior probability than that found by `BFGS`, so we repeated the sampling procedure once more starting from the new MAP values. The Gelman–Rubin $\hat{R}$ statistic (Gelman & Rubin 1992) was less than 1.003 for all parameters, indicating that the samplers had converged, and the number of effectively independent samples was large enough to ensure negligibly small sampling errors. The results are summarized in Table 2, and detailed plots showing the model fits to the TESS and ground-based data sets are shown in Figures 6, 7, 8, and 9.

Table 1
Main Identifiers, Equatorial Coordinates, Proper Motion, Parallax, Optical and Infrared Magnitudes, and Fundamental Parameters of TOI-1696

Parameter	Value	Source
Main identifiers		
TIC	470381900	TIC v8[a]
2MASS	J04210733+4849116	ExoFOP[a]
WISE	J042107.34+484911.5	ExoFOP[a]
UCAC4	695-028795	ExoFOP[a]
Gaia EDR3	270260649602149760	Gaia EDR3[b]
Equatorial coordinates, parallax, and proper motion		
R.A. (J2015.5)	$04^h21^m07\overset{s}{.}36$	Gaia EDR3[b]
Decl. (J2015.5)	$+48\,°\,49'11\overset{''}{.}38$	Gaia EDR3[b]
π (mas)	15.4752 ± 0.0345	Gaia EDR3[b]
μ_α (mas yr^{-1})	12.8726 ± 0.0345	Gaia EDR3[b]
μ_δ (mas yr^{-1})	-19.0463 ± 0.0269	Gaia EDR3[b]
Optical and near-infrared photometry		
TESS	13.9664 ± 0.00730068	TIC v8[a]
G	15.3056 ± 0.0028	Gaia EDR3[b]
B_p	17.0511 ± 0.0051	Gaia EDR3[b]
R_p	14.0457 ± 0.0039	Gaia EDR3[b]
B	18.467 ± 0.162	ExoFOP[a]
V	16.82 ± 1.133	ExoFOP[a]
J	12.233 ± 0.023	2MASS[c]
H	11.604 ± 0.031	2MASS[c]
Ks	11.331 ± 0.023	2MASS[c]
*W*1	11.134 ± 0.023	AllWISE[c]
*W*2	10.984 ± 0.021	AllWISE[c]
*W*3	10.71 ± 0.11	AllWISE[d]
*W*4	$8.748\pm$	AllWISE[d]
Fundamental parameters		
$T_{\rm eff}$(K)	3185 ± 76	This work
log g(cgs)	4.959 ± 0.026	This work
[Fe/H](dex)	0.336 ± 0.060	This work
$M_\star(M_\odot)$	0.255 ± 0.0066	This work
$R_\star(R_\odot)$	0.2775 ± 0.0080	This work
$\rho_\star$(g cm^{-3})	$16.8^{+1.5}_{-1.4}$	This work
distance (pc)	65.03 ± 0.36	This work
Luminosity ($L_\odot$)	$0.00711^{+0.00083}_{-0.00075}$	This work

Notes.
[a] ExoFOP (2019).
[b] Stassun & Torres (2021).
[c] Skrutskie et al. (2006).
[d] Cutri et al. (2021).

[44] https://docs.pymc.io
[45] https://docs.exoplanet.codes
[46] Implemented in https://github.com/john-livingston/limbdark.

Table 2
Results of Joint Fit to the TESS and Ground-based Transit Data Sets

Parameter	Value
Primary transit parameters	
$M_\star$ [$M_\odot$]	0.255 ± 0.007
$R_\star$ [$R_\odot$]	0.277 ± 0.008
T_0 [BJD]	$2458834.20115 \pm 0.00058$
P [days]	2.500311 ± 0.000004
b	$0.59^{+0.03}_{-0.04}$
$R_P/R_\star$ (T)	0.0952 ± 0.0062
$R_P/R_\star$ (V)	0.1021 ± 0.0057
$R_P/R_\star$ (g)	$0.1036^{+0.0060}_{-0.0068}$
$R_P/R_\star$ (r)	0.1053 ± 0.0034
$R_P/R_\star$ (i)	0.1023 ± 0.0020
$R_P/R_\star$ (z)	0.1026 ± 0.0020
$R_P/R_\star$	0.1025 ± 0.0014[a]
Limb darkening parameters	
u_1 (T)	0.16 ± 0.01
u_2 (T)	0.48 ± 0.01
u_1 (V)	0.48 ± 0.02
u_2 (V)	0.30 ± 0.01
u_1 (g)	0.49 ± 0.01
u_2 (g)	0.31 ± 0.01
u_1 (r)	0.50 ± 0.01
u_2 (r)	0.25 ± 0.01
u_1 (i)	0.37 ± 0.01
u_2 (i)	0.28 ± 0.01
u_1 (z)	0.24 ± 0.01
u_2 (z)	0.36 ± 0.01
Derived parameters	
R_p [$R_\oplus$]	3.09 ± 0.11[a]
a [au]	0.0229 ± 0.0002
T_{eq} [K]	489 ± 13[b]
T_{14} [hours]	1.00 ± 0.01

Notes.
[a] Derived from achromatic transit model fit.
[b] Assuming a Bond albedo of 0.3.

3.4.5. Achromatic Model

We did not detect any significant wavelength dependence of the transit depth (see Figure 10), which rules out many plausible false-positive scenarios involving eclipsing binaries (see Section 3.6 for more details). Having established that the transit depth is achromatic, we robustly determined the planet radius by conducting a second fit with a single $R_P/R_\star$ parameter for all data sets. This fit resulted in a final value of $R_P/R_\star = 0.1025 \pm 0.0014$, corresponding to an absolute radius of $3.09 \pm 0.11\,R_\oplus$, and all other parameters were unchanged.

3.5. Companion Mass Constraints

To put a limit on the mass of TOI-1696.01, we fit an RV model with a circular orbit to the RV data from Subaru/IRD. Between the *H*-band and the *YJ*-band spectra obtained with IRD, we opted to use the *H*-band spectra for RV analysis because of its higher S/N.[47] The data observed on 2021 January 29 were excluded because of the possibility of an RV offset, as there was a gap of 8 months relative to the succeeding observations. We also removed any data with the clouds passing, which can cause systematic errors. The final data set consisted of 9 RV measurements from 2021 September 29 to 2022 January 8.

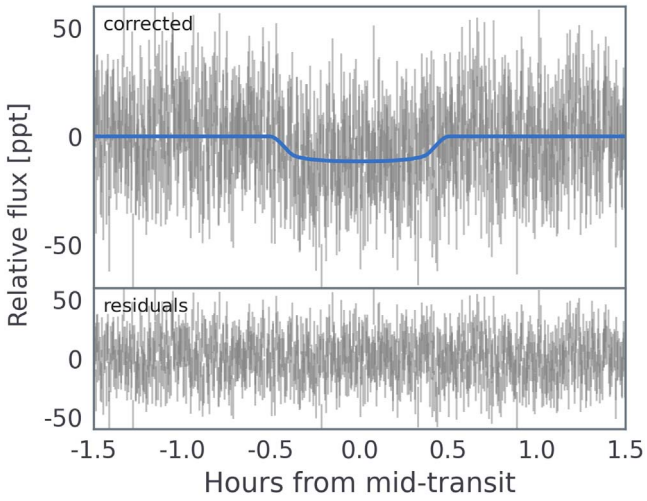

Figure 6. Phase-folded TESS light curve after removing the best-fit GP noise model, with the best-fit transit model (blue) from our joint analysis of the TESS and ground-based light curves.

We used the RV model included in `PyTransit` (Parviainen 2015), which we simplified to have five free parameters: phase-zero epoch T_0, period, RV semi-amplitude, RV zero-point, and RV jitter term. Here, we defined the word RV jitter term' as a parameter that describes the amplitude of white-noise-like scatter due to the systematics. For T_0 and the period, we put Gaussian priors using T_0 and the period derived from the transit analysis. For the other parameters we put wide uniform priors. We ran the built-in Differential Evolution optimizer and then sampled the parameters with Markov Chain Monte Carlo (MCMC) using 30 walkers and 10^4 steps. We use the following equation to derive the planet mass,

$$M_p = \left(\frac{PM_\star^2}{2\pi}\right)^{1/3} \frac{K(1-e^2)^{1/2}}{\sin(i)}, \quad (1)$$

where M pis the planet mass, $M_\star$ is the star mass, P is the orbital period, K is the RV semi-amplitude, e is the eccentricity (fixed to zero), and i is the inclination (fixed to 90°). To propagate uncertainties, we use the posteriors for $M_\star$ and P from previous analyses.

In Figure 11 we plot Keplerian orbital models corresponding to different masses encompassing the 68th, 95th, and 99.7th percentiles of the semi-amplitude posterior distribution. The 2σ upper limit is $48.8\,M_\oplus$, which places the companion 2 orders of magnitude below the deuterium burning mass limit. The best-fit semi-amplitude is $K = 14.4\ \mathrm{ms}^{-1}$, which corresponds to a mass of $M_p = 12.3 M_\oplus$, and the best-fit jitter value is $\sigma_K = 62\ \mathrm{m\,s}^{-1}$.

We calculated an expected planetary mass of $\sim 8\,M_\oplus$ with `MREXO`,[48] which uses a mass–radius relationship calibrated for planets around M dwarfs (Kanodia et al. 2019). This mass corresponds to a semi-amplitude of $9.4\ \mathrm{m\,s}^{-1}$, but the observed

[47] There have been reports of unpredictable systematic errors caused by persistence light on the detector in the *H* band, especially when bright stars are observed before fainter stars. We checked the objects observed before TOI-1696 and found that none were more than 1.2 mag brighter in the *H* band, i.e., persistence light is not likely to be a problem with these data.

[48] https://github.com/shbhuk/mrexo

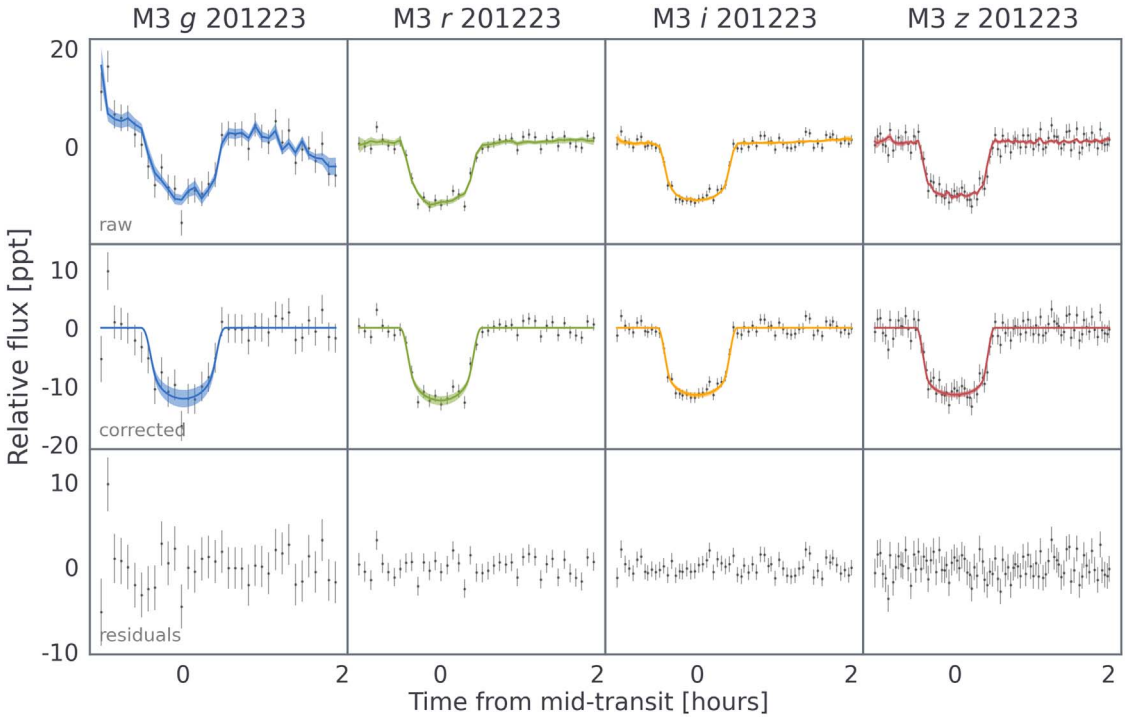

Figure 7. Transit model fit to the MuSCAT3 (M3) data from 2020 December 23, ordered column-wise per bandpass. The top row shows the raw data with the transit and systematics model, the middle row shows the systematics-corrected data with only the transit model, and the bottom row shows the residuals from the fit. The colors of the model correspond to the photometric bandpass of each data set; see also Figure 10.

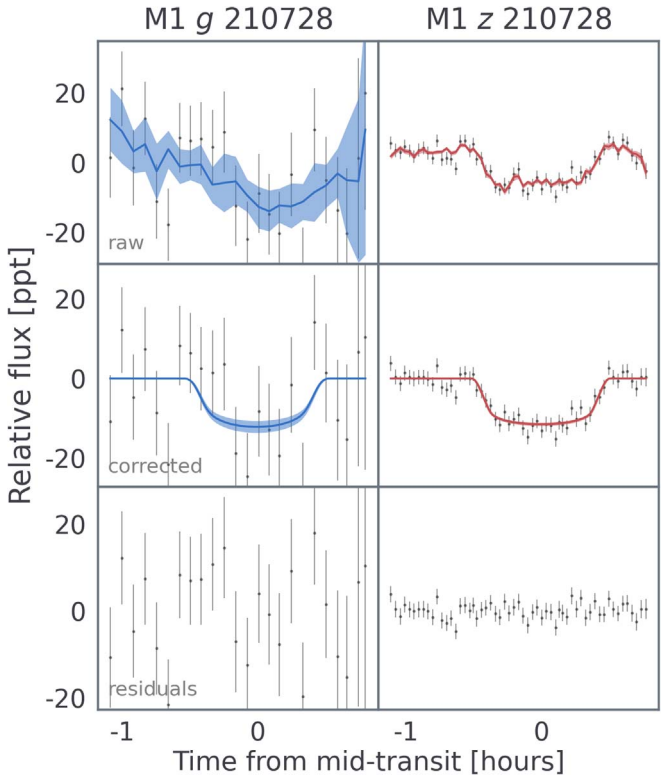

Figure 8. Same as Figure 7, but for the MuSCAT (M1) data from 2021 July 28.

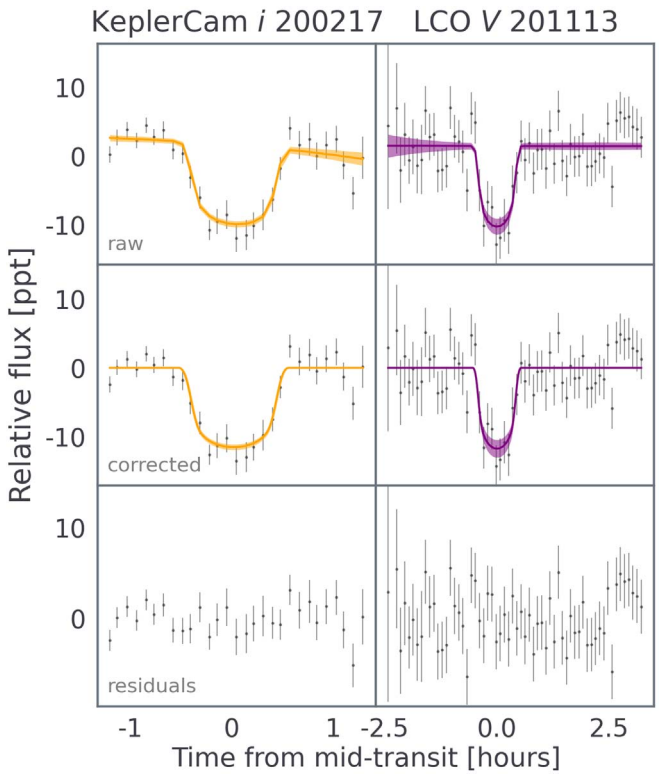

Figure 9. Same as Figure 7, but for the KeplerCam and LCO data from 2020 February 17 and 2021 November 13, respectively.

RV data exhibit significantly larger variability ($\sigma \approx 52$ m s^{-1}). We interpret this variability as being responsible for the large jitter value found by the fit, which suggests it is out-of-phase with TOI-1696.01. As the star appears to be quiet, one explanation for this signal is the existence of an additional (possibly nontransiting) planet, but more RV measurements would be required to determine if this is the case. Furthermore, if such a planet were dynamically interacting with TOI-1696.01, then this could help explain TOI-1696.01's location

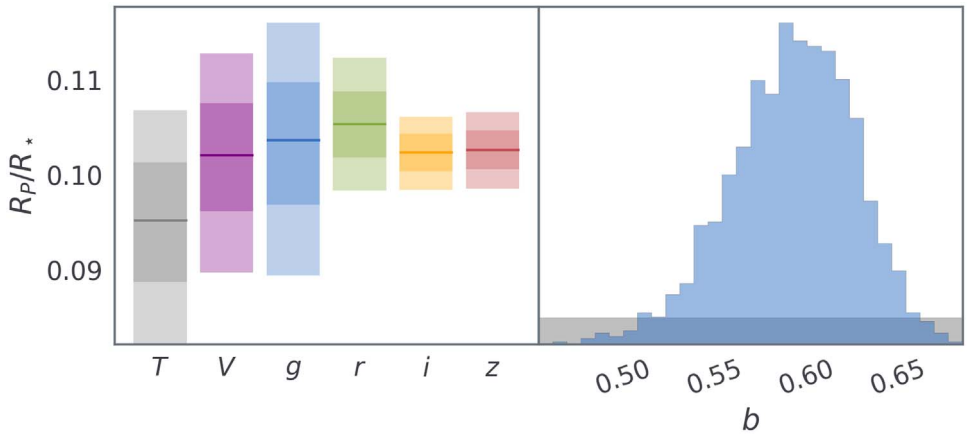

Figure 10. Posteriors of the planet-to-star radius ratio ($R_P/R_\star$) in each bandpass (left) and impact parameter (right) from the joint fit to the TESS data and the ground-based data shown in Figures 7, 8, and 9; the gray shaded region in the right panel represents the uniform prior used in the fit, while the blue histogram is the posterior.

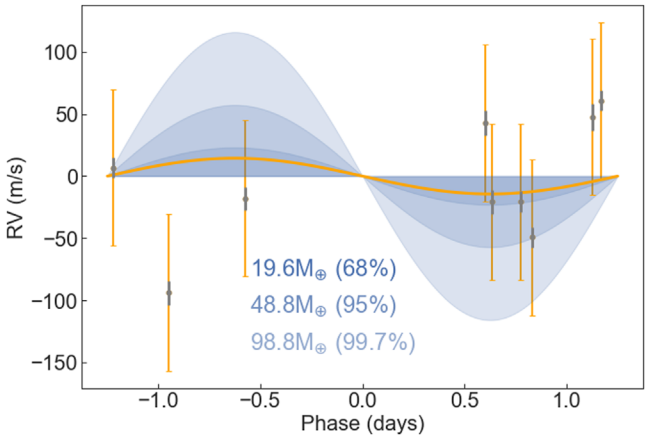

Figure 11. Phase-folded RVs with Keplerian models corresponding to the 1σ, 2σ, and 3σ mass upper limits. The gray points with the error bars show the errors estimated from the data-processing method described in Section 2.8. The error bars in orange show the original errors + jitter term value of 62 m s^{-1} (added in quadrature) from the best-fit RV model (orange line, best $M_p = 12.3 M_\oplus$).

in a sparsely populated part of the period–radius plane (see Section 4).

3.6. Eliminating False-positive Scenarios

A number of astrophysical scenarios can mimic the transit signal detected from TESS photometry, including an eclipsing binary (EB) with a grazing transit geometry, a hierarchical EB (HEB), and a diluted eclipse of a background (or foreground) EB (BEB) along the line of sight of the target. In the following, we will examine the plausibility of each scenario.

First, the renormalized unit weight error (RUWE) from Gaia EDR3 is 1.12, which suggests that TOI-1696 is single (Belokurov et al. 2020). We can also rule out the EB scenario based on the analysis of the IRD CCF in Section 3.2, and the mass constraint derived in Section 3.1.1. Finally, the absence of any wavelength dependence of the transit depth from our chromatic transit analysis (Section 3.4) is incompatible with contamination from a star of different spectral type (color) than the host star, the details of which are discussed in Appendix B. In the absence of dilution, the measured radius of $3.09 \pm 0.11\ R_\oplus$ ($0.27\ R_{\rm Jup}$) equals the true radius, which makes it significantly smaller than the lower limit of $0.8\ R_{\rm Jup}$ expected for brown dwarfs (Burrows et al. 2011).

Grazing transit geometries can also be eliminated, as the impact parameter is constrained to $b < 0.7$ at the 99% level based on our transit and contamination analyses. The apparent boxy shape of our follow-up light curves is in stark contrast with the V-shaped transit expected for grazing orbits. Hence, grazing EB scenario is ruled out.

Moreover, we can constrain the classes of HEBs that can reproduce the observed transit depth and shape using our multiband observations. We aim to compute the eclipse depths for a range of plausible HEBs in the bluest and reddest bandpasses where they are expected to vary significantly. We adopt the method presented in Bouma et al. (2020) to perform the calculation taking into account nonzero impact parameter, the details of which are discussed in Appendix C. Comparing the simulated eclipse depths with the observed depth in each band, we found that there is no plausible HEB configuration explored in our simulation that can reproduce the observed depths in multiple bands simultaneously. Hence, the HEB scenario is ruled out.

Although, TOI-1696's probability of being a BEB is very high a priori given its location at the galactic plane, we argue in the following that the BEB scenario is extremely unlikely. Our MuSCAT3 observation can resolve the signal down to 3″, which represents the maximum radius within which the signal must originate. Furthermore, our high-resolution speckle imaging ruled out any nearby star and blended sources down to 0.″1 at a delta mag of 4.5. We checked archival images taken more than 60 yr apart, but the proper motion of TOI-1696 is not enough to obtain a clear view along the line of sight of the star. However, we can use statistical arguments to estimate the probability of a chance-aligned star. To do this, we use the population synthesis code TRILEGAL[49] (Girardi et al. 2005), which can simulate the Galactic stellar population along any line of sight. Given the position of TOI-1696, we found a probability of 5×10^{-8} to find a star brighter than $T = 16$,[50] within an area equal to the smallest MuSCAT3 photometric aperture (aperture radius = 3″). Assuming all such stars are binary and preferentially oriented edge-on to produce eclipses

[49] http://stev.oapd.inaf.it/cgi-bin/trilegal

[50] T denotes the TESS bandpass. The maximum delta magnitude was computed using $\mathrm{dT} = -2.5\ \log_{10}(\mathrm{depth})$, which translates to the magnitude that can produce a 100% eclipse.

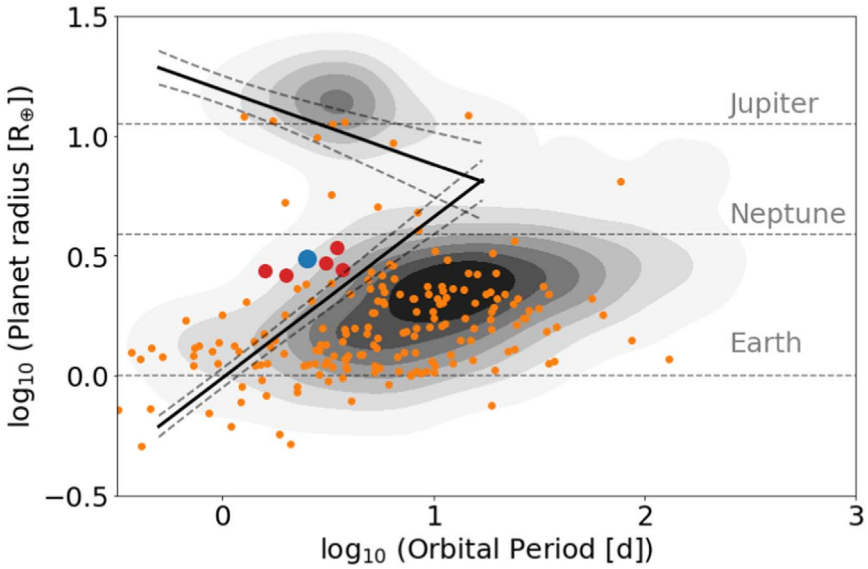

Figure 12. TOI-1696 b (blue point) in the context of known transiting planets (contours). TOI-1696 b appears to be within or close to the boundaries of the Neptunian desert (solid black lines) in the period–radius plane defined by Mazeh et al. (2016). The dashed lines refer to the boundaries' uncertainty regions. Also shown are planets (orange points) orbiting M dwarfs ($T_{\rm eff} < 3800$ K) and the five planets (red points) most similar in this parameter space to TOI-1696 b: K2-25 b, K2-320 b, GJ 1214b, TOI-269 b, and TOI-2406b.

with period and depth consistent with the TESS detection, then this can represent a very conservative upper limit of a BEB scenario. Despite the small probability of a BEB based on the trivial star counting argument, we discuss relevant tools in the following section for a more thorough statistical modeling.

3.7. Statistical Validation

Here we quantify the false-positive probability (FPP) of TOI-1696.01 using the Python package `Vespa` and `Triceratops` (Morton 2015a; Giacalone & Dressing 2021), the details of which are discussed in Appendix D. Although we were able to rule out the classes of EB, BEB, and HEB in Section 3.6, we ran `Vespa` considering all these scenarios for completeness and computed a formal FPP $< 1 \times 10^{-6}$, which robustly quantifies TOI-1696.01 as a statistically validated planet. Additionally, we validated TOI-1696.01 using `Triceratops`and found FPP $= 2 \times 10^{-3}$. Giacalone et al. (2021) noted that TOIs with FPP < 0.015 have a high enough probability of being bona fide planets to be considered validated. The low FPPs calculated using `Vespa` and `Triceratops` added further evidence to the planetary nature of TOI-1696.01. We now refer to the planet as TOI-1696 b in the remaining sections.

4. Discussion

4.1. The Nature of the Planet

Here, we consider the nature of TOI-1696 b by placing it in context with the population of known exoplanets[51] (NASA Exoplanet Science Institute 2020). Figure 12 shows a radius versus period diagram, indicating that there are only a handful of planets with similar characteristics to TOI-1696 b. The measured planetary radius $R_{\rm p}$ of $3.09 \pm 0.11\,R_{\oplus}$ and the orbital period P of 2.50031 ± 0.00001 days, places it securely within the bounds of the Neptunian desert as defined by Mazeh et al. (2016). The region occupied by TOI-1696 remains sparsely populated despite recent discoveries of TESS planets within the Neptunian desert (e.g., Murgas et al. 2021; Brande et al. 2022).

It should be noted that the Neptunian desert was originally determined based on a population of planets orbiting mainly solar-type stars from the Kepler mission. Because TOI-1696 is an M dwarf, the incident flux at a given orbital separation will be less than for solar-type stars. Nevertheless, we emphasize that the target exists in a sparsely populated region of the parameter space, despite the large number of planets discovered around M dwarfs since the Kepler mission (i.e., from K2 and TESS). For example, if we limit the comparison to the 279 confirmed planets around M dwarfs with $T_{\rm eff}$ below 3800 K, only 14 planets have been found so far with orbital periods shorter than 10 days and planetary radii in the range of $2.5R_{\oplus} < R_{\rm p} < 5\,R_{\oplus}$. As shown in Figure 12, TOI-1696 b is similar to K2-25 b (Mann et al. 2016), K2-320 b (Castro González et al. 2020), GJ 1214 b (Charbonneau et al. 2009), TOI-269 b (Cointepas et al. 2021), and TOI-2406 b (Wells et al. 2021) in terms of the orbital period and radius. In particular, TOI-2406b appears most similar to TOI-1696 b as it orbits around a mid-M dwarf with an effective temperature of 3100 ± 75, and has a radius of $2.94 \pm 0.17\,R_{\oplus}$ and orbital period of 3.077 days. TOI-2406 is also thought to be relatively old without any activity signal. As both TOI-1696 b and TOI-2406b are excellent targets for detailed characterization studies, together they may provide unique insights into this class of planet. There is also some similarity between TOI-1696 b and the Neptunian Desert planets orbiting young host stars, such as au Mic b and c, K2-25 b, K2-95 b, and K2-264 b. It has been suggested that these planets may have inflated radii and could possibly still be undergoing atmospheric mass loss (e.g., Mann et al. 2016). Further study of TOI-1696 b could reveal whether its similarity to these planets (despite being older) is only superficial, or if it is indicative of an inflated radius.

[51] Based on a query of the NASA Exoplanet Archive "Confirmed Planets" table on 2022 January 31, https://exoplanetarchive.ipac.caltech.edu/.

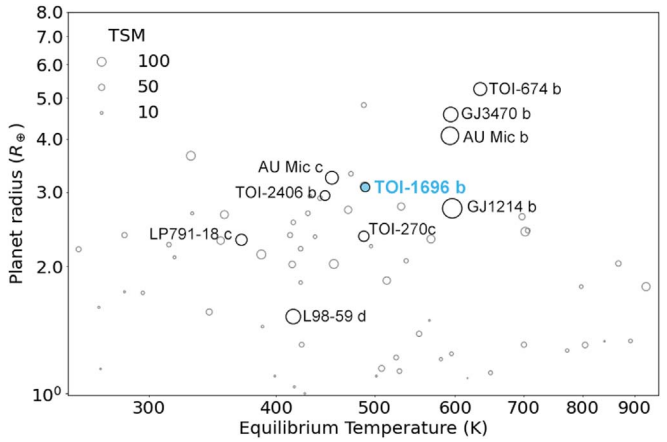

Figure 13. Planetary equilibrium temperature vs. radius for TOI-1696 b and other planets with $Rp < 10R_\oplus$, with the host stars having $T_{\rm eff} < 3800$K and $H < 11$mag. The point size represents the calculated TSM values. Data points with a planet name beside them are those with a higher TSM values than the target.

4.2. Prospects for Transmission Spectroscopy

Given the rarity of this planet, it would be useful to assess its prospects for future atmospheric observations to understand its formation and evolution. In particular, the relatively large size of the planet compared to its host star makes it a good candidate for transmission spectroscopy. Using Equation (1) in Kempton et al. (2018), we calculated the transmission spectroscopy metric (TSM) of TOI-1696 b from its mass, radius, equilibrium temperature, stellar radius, and J-band magnitude. We used the values in Tables 1 and 2, and assumed a mass of $8\,M_\oplus$ estimated by MREx○. The derived TSM value of TOI-1696 b is 105.6. For reference, Kempton et al. (2018) suggested that planets with TSM > 90 are ideal targets for atmospheric follow-up.

For comparison, we calculated the TSM for the known population of transiting M dwarf planets. We selected planets with $T_{\rm eff} < 3800$ K, $R_{\rm p} < 10\,R_\oplus$, and H < 11mag.[52] For planets without mass measurements, we assumed the masses predicted by MREx○. For planets without an equilibrium temperature, we estimated it from the semimajor axis and the host star's effective temperature (assuming zero albedo). Figure 13 shows the computed TSM values for the selected samples of planets. The TSM of TOI-1696 b places it in the top 10, making it one of the best targets for future atmospheric investigations.

4.3. Existence of a Primordial Atmosphere

Up to this point in the section, the discussion has been based on the assumption that the target has an atmosphere. Usually it is thought that planets above the so-called radius gap can retain their atmospheres (Weiss & Marcy 2014; Rogers 2015). However, does TOI-1696 b actually have a H_2/He atmosphere? Here we study the atmospheric mass that TOI-1696 b can retain after ~8 Gyr under a stellar XUV irradiation. The mass of TOI-1696 b remains poorly constrained as discussed in Section 3.5. We modeled TOI-1696 b as a rocky planet with Earth-like core compositions ($MgSiO_3$:Fe = 7:3) in the mass range from $0.5\,M_\oplus$ to $20\,M_\oplus$. The silicate mantle and iron core were described by the third-order Birch–Murnagham equation of state (EoS) for $MgSiO_3$ perovskite (Karki et al. 2000; Seager et al. 2007) and the Vinet EoS for ϵ-Fe (Anderson et al. 2001), respectively. The Thomas–Fermi–Dirac EoS (Salpeter & Zapolsky 1967) was applied to high-pressure EoS for $MgSiO_3$ at $P \geqslant 4.90$ TPa and Fe at $P \geqslant 2.09 \times 10^4$ GPa (Seager et al. 2007; Zeng & Sasselov 2013). The pressure and temperature in a H_2/He envelope were calculated using the SCvH EoS (Saumon et al. 1995).

We computed the thermal evolution of TOI-1696 b with a H_2/He atmosphere by calculating its interior structure in hydrostatic equilibrium for ~8 Gyr and calculated its mass-loss process. The initial mass fraction of a H_2/He atmosphere for a rocky planet ranges from 0.001% to 30% of its core mass. The energy-limited hydrodynamic escape (Watson et al. 1981) controls the mass-loss rate given by

$$\frac{dM_{\rm p}}{dt} = -\eta \frac{R_{\rm p}^3 L_{\rm XUV}(t)}{4GM_{\rm p}a^2K_{\rm tide}}, \quad (2)$$

where η is the heating efficiency due to stellar XUV irradiation, $L_{\rm XUV}$ is the stellar XUV luminosity, G is the gravitational constant, and $R_{\rm p}$ is the planetary radius (Erkaev et al. 2007). As the heating efficiency for a hydrogen-rich upper atmosphere was lower than 20% (Shematovich et al. 2014; Ionov & Shematovich 2015), we adopted $\eta = 0.1$. $K_{\rm tide}$ is the reduction factor of a gravitational potential owing to the effect of a stellar tide:

$$K_{\rm tide}(\xi) = 1 - \frac{3}{2\xi} + \frac{1}{2\xi^3} < 1, \quad \xi = \frac{R_{\rm H}}{R_{\rm p}}, \quad (3)$$

where $R_{\rm H}$ is the Hill radius. The XUV luminosity ($L_{\rm XUV}$) of TOI-1696 followed from the X-ray-to-bolometric luminosity relations of M-type stars (Jackson et al. 2012), where we adopted the current luminosity of TOI-1696 as its bolometric luminosity. We also considered a $10L_{\rm XUV}$ model because of the large uncertainty in $L_{\rm XUV}$ of young M dwarfs.

Figure 14 shows the initial H_2/He atmosphere of a TOI-1696 b-like planet that reproduces the radius of $3.09 \pm 0.11 R_\oplus$ at the current location (i.e., $T_{\rm eq} = 489 \pm 13$ K) after the mass loss driven by the standard XUV radiation ($L_{\rm XUV}$: blue) and 10 times higher one ($10L_{\rm XUV}$: red). The gray region shows the H_2/He atmospheric mass fraction of TOI-1696 b with a rocky core that satisfies its observed radius. The observed radius of TOI-1696 b favors the existence of a H_2/He atmosphere atmosphere with $\gtrsim$3 wt% (a percentage by weight) unless its core contains icy material. We find that TOI-1696 b can possess the H_2/He atmosphere for 8 Gyr if its core mass is larger than ~1.5 $M_\oplus$ (~4 $M_\oplus$ for $10L_{\rm XUV}$ models). We rule out the possibility that TOI-1696 b with a rocky core initially had a H_2/He atmosphere of $\lesssim$3%. Also, TOI-1696 b with mass of $\gtrsim$10 $M_\oplus$ can retain almost all the H_2/He atmosphere accreted from a disk. These suggest that if TOI-1696 b has a core of $\gtrsim$1.5–4 $M_\oplus$, it is likely to be a sub-Neptune with a H_2/He atmosphere.

5. Conclusions

TESS found transit signals of a sub-Neptune planet orbiting a mid-M dwarf TOI-1696. To validate and characterize the planetary system, we conducted follow-up observations of this

[52] Based on a query of the NASA Exoplanet Archive Confirmed Planets table (NASA Exoplanet Science Institute 2020) as of 2022 January 31.

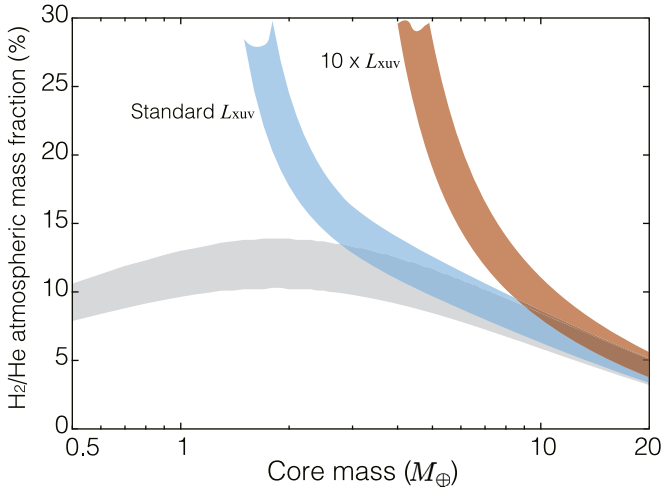

Figure 14. Initial H_2/He atmospheric mass fraction of a TOI-1696 b-like planet that satisfies the radius of $3.09 \pm 0.11\ R_\oplus$ and $T_{eq} = 489 \pm 13$ K after photoevaporative mass loss for 8 Gyr under the standard XUV radiation field (L_{XUV}) and $10L_{XUV}$. The gray region shows the H_2/He atmospheric mass fraction that reproduces the observed radius of TOI-1696 b with a rocky core.

system including ground-based transit photometry, high-resolution imaging, and high- and medium-resolution spectroscopy.

We have used several methods to determine the stellar parameters based on the results of the spectroscopic observations, and have confirmed that the results are consistent. The host star, TOI-1696, is a M-type star with a $M_\star$ at $0.255 \pm 0.0066\ M_\odot$ and $T_{\rm eff}$ at 3185 ± 76 K.

The fact that this target is located near the Galactic plane makes validation difficult. We used the results obtained to rule out various scenarios that could reproduce the TESS signal (grazing EB, HEB, and BEB).

The validated planet, TOI-1696 b is a Sub-Neptune size planet with the radius at $3.09\ R_\oplus$ and rotation period at 2.5 days, which is located in the Neptunian desert. To see its atmospheric properties, we calculated how much of the atmosphere it currently retains, and found the planet likely to retain the H_2/He atmosphere if it has a core of $>$1.5–4 $M_\oplus$. In order to statistically evaluate the feasibility of transmission spectroscopy on this planet, we have also calculated and compared the TSM and concluded that this target is one of the planets with the best prospects for atmospheric detection among the currently known sub-Neptune-sized planets. In addition, future RV observations with high-resolution infrared spectrographs such as IRD will allow us to place more substantial limits on the planetary mass.

Funding for the TESS mission is provided by NASA's Science Mission Directorate. We acknowledge the use of public TESS data from pipelines at the TESS Science Office and at the TESS Science Processing Operations Center. This research has made use of the Exoplanet Follow-up Observation Program website, which is operated by the California Institute of Technology, under contract with the National Aeronautics and Space Administration under the Exoplanet Exploration Program. Resources supporting this work were provided by the NASA High-End Computing (HEC) Program through the NASA Advanced Supercomputing (NAS) Division at Ames Research Center for the production of the SPOC data products. This paper includes data collected by the TESS mission that are publicly available from the Mikulski Archive for Space Telescopes (MAST).

This work makes use of observations from the Las Cumbres Observatory global telescope network. Some of the observations in the paper are based on observations made with the MuSCAT3 instrument, developed by the Astrobiology Center and under financial supports by JSPS KAKENHI (JP18H05439) and JST PRESTO (JPMJPR1775), at Faulkes Telescope North on Maui, HI, operated by the Las Cumbres Observatory.

This research is in part based on data collected at the Subaru Telescope, which is operated by the National Astronomical Observatory of Japan, and at the Gemini North telescope, located within the Maunakea Science Reserve and adjacent to the summit of Maunakea. We are honored and grateful for the opportunity of observing the Universe from Maunakea, which has cultural, historical, and natural significance in Hawaii. Our data reductions benefited from `PyRAF` and `PyFITS`, which are the products of the Space Telescope Science Institute, which is operated by AURA for NASA. This research made use of Astropy,[53] a community-developed core Python package for Astronomy (Astropy Collaboration et al. 2013, 2018). Some of the observations in the paper made use of the High-Resolution Imaging instrument(s) Alopeke. Alopeke was funded by the NASA Exoplanet Exploration Program and built at the NASA Ames Research Center by Steve B. Howell, Nic Scott, Elliott P. Horch, and Emmett Quigley. Alopeke (and/or Zorro) was mounted on the Gemini North (and/or South) telescope of the international Gemini Observatory, a program of NSF's NOIRLab, which is managed by the Association of Universities for Research in Astronomy (AURA) under a cooperative agreement with the National Science Foundation on behalf of the Gemini partnership: the National Science Foundation (United States), National Research Council (Canada), Agencia Nacional de Investigación y Desarrollo (Chile), Ministerio de Ciencia, Tecnología e Innovación (Argentina), Ministério da Ciência, Tecnologia, Inovações e Comunicações (Brazil), and Korea Astronomy and Space Science Institute (Republic of Korea). Some of the observations in this paper made use of the Infrared Telescope Facility, which is operated by the University of Hawaii under contract 80HQTR19D0030 with the National Aeronautics and Space Administration. The IRTF observations were collected under the program 2020B115 (PI: S. Giacalone). This work has made use of data from the European Space Agency (ESA) mission Gaia (https://www.cosmos.esa.int/gaia), processed by the GaiaData Processing and Analysis Consortium (DPAC; https://www.cosmos.esa.int/web/gaia/dpac/consortium). Funding for the DPAC has been provided by national institutions, in particular the institutions participating in the Gaia Multilateral Agreement. This work is supported by Grant-in-Aid for JSPS Fellows, grant No. JP20J21872, JSPS KAKENHI grant Nos. JP20K14518, JP19K14783, JP21H00035, JP18H05439, JP18H05439, JP20K14521, JP17H04574, JP21K20376, JP21K13975, JP18H05442, JP15H02063, JP22000005, and JP21K20388, SATELLITE Research from Astrobiology Center (grant No. AB031010, AB022006, and AB031014), and JST CREST grant No. JPMJCR1761.

[53] http://www.astropy.org

E.E.-B. acknowledges financial support from the European Union and the State Agency of Investigation of the Spanish Ministry of Science and Innovation (MICINN) under grant PRE2020-093107 of the Pre-Doc Program for the Training of Doctors (FPI-SO) through FSE funds.

Software: AstroImageJ (Collins et al. 2017), LCOGT BANZAI pipeline (McCully et al. 2018), PyMC3 (Salvatier et al. 2016), exoplanet (Foreman-Mackey et al. 2019), starry (Luger et al. 2019), celerite2 (Foreman-Mackey et al. 2017; Foreman-Mackey 2018), PyTransit (Parviainen 2015), Vespa (Morton 2015a), Isochrones(Morton 2015b), Triceratops (Giacalone & Dressing 2021), and astropy (Astropy Collaboration et al. 2013, 2018).

Appendix A
Detailed Methods of Stellar Parameter Estimation

A.1. Abundances of Eight Metal Elements from IRD Spectra

We calculate the abundance of seven elements in addition to iron from IRD spectra. We used 28 lines in total caused by neutral atoms of Na, Mg, Ca, Ti, Cr, Mn, and Fe and singly ionized Sr. The detailed procedures of abundance analysis and error estimation are described in Ishikawa et al. (2020). Figure A1 shows the final values of abundance after the iteration. From the final values of the abundances of the eight elements, [M/H] was determined by calculating the average weighted by the inverse of the square of their estimated errors.

A.2. Estimation of the Stellar Radius and Mass: SED Fitting

As an independent determination of the basic stellar parameters, we performed an analysis of the broadband spectral energy distribution (SED) of the star together with the Gaia EDR3 parallax (Stassun & Torres 2021), in order to determine an empirical measurement of the stellar radius, following the procedures described in Stassun & Torres (2016); Stassun et al. (2017, 2018). We pulled the JHK_S magnitudes from 2MASS, the W1–W3 magnitudes from the Wide-field Infrared Survey Explorer (WISE), and the *grizy* magnitudes from the Panoramic Survey Telescope and Rapid Response System. Together, the available photometry spans the full stellar SED over the wavelength range 0.4–10 μm (see Figure A2).

We performed a fit using NextGen stellar atmosphere models (Hauschildt et al. 1999), with the effective temperature ($T_{\rm eff}$) and metallicity ([Fe/H]) constrained from the spectroscopic analysis. The remaining free parameter is the extinction A_V, which we fixed at zero due to the star's proximity. The resulting fit (Figure A2) has a reduced χ^2 of 1.7. Integrating the (unreddened) model SED gives the bolometric flux at Earth, $F_{\rm bol} = 5.20 \pm 0.25 \times 10^{-11}$ erg s^{-1} cm^{-2}. Taking the $F_{\rm bol}$ and $T_{\rm eff}$ together with the Gaia parallax, gives the stellar radius, $R_\star = 0.276 \pm 0.015$ R$_\odot$. We used the $T_{\rm eff}$ and [Fe/H] values from spectroscopic results as priors for the parameter estimation.

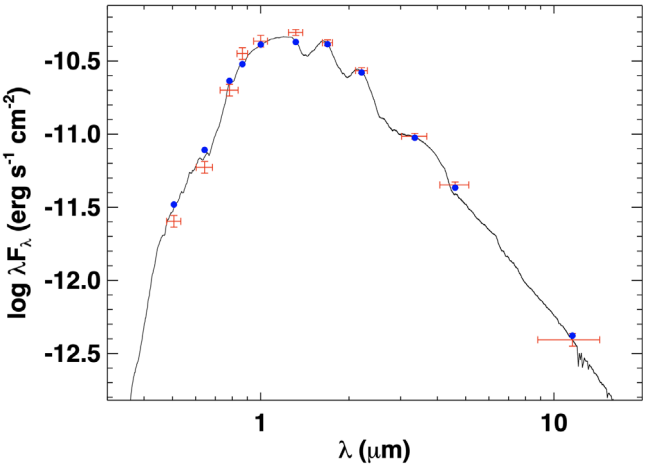

Figure A2. SED of TOI-1696. Red symbols represent the observed photometric measurements, where the horizontal bars represent the effective width of the passband. Blue symbols are the model fluxes from the best-fit NextGen atmosphere model (black).

In addition, we estimated the stellar mass from the empirical relations of Mann et al. (2019), giving $M_\star = 0.279 \pm 0.014$ M$_\odot$. Finally, the radius and mass together imply a mean stellar density of $\rho_\star = 18.79 \pm 3.26$ g cm^{-3}.

A.3. Stellar Parameter Comparison

In addition to the methods described above, we used the Python package `isochrones`, which calculates stellar parameters from the stellar evolution models. The three methods are not fully independent, as some of them use the same relations such as mass derivation from Mann et al. (2019), but comparing three results are useful to confirm the results are

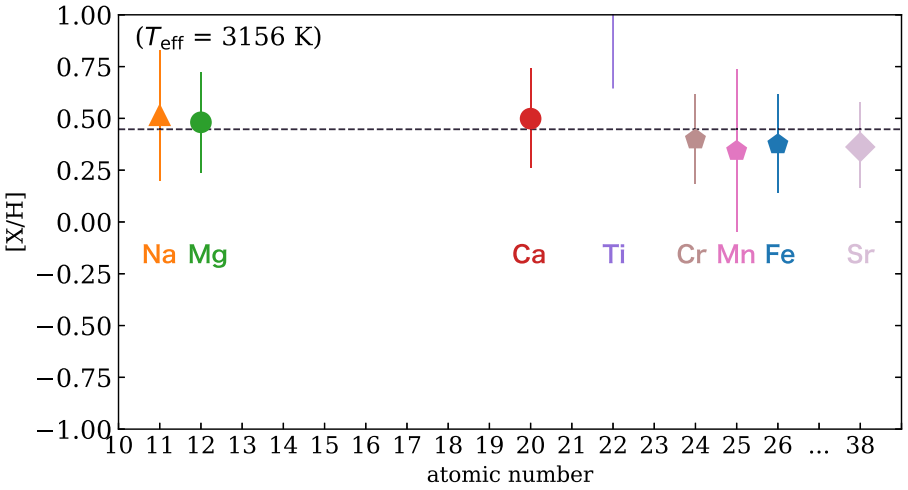

Figure A1. Metallicity values derived from the IRD spectrum. The horizontal dashed line corresponds to the weighted average [M/H].

Table A1
Stellar Parameters Derived from Empirical Relations (Method 1; Section 3.1.3), SED Fitting (Method 2; Appendix A.2), and `isochrones` (Method 3; Appendix A.3)

Parameter	Method 1	Method 2	Method 3
$T_{\rm eff}$ (K)	⋯	3130 ± 75	3159 ± 40
[Fe/H] (dex)	⋯	0.2 ± 0.3	$0.232^{+0.035}_{-0.038}$
$M_\star$ ($M_\odot$)	0.255 ± 0.0066	0.279 ± 0.014	$0.276^{+0.006}_{-0.005}$
$R_\star$ ($R_\odot$)	0.2775 ± 0.0080	0.280 ± 0.014	0.291 ± 0.005
$\log g$ (cgs)	4.959 ± 0.026	4.990 ± 0.049	$4.955^{+0.008}_{-0.007}$
$\rho_\star$ (g cm^{-3})	$16.8^{+1.5}_{-1.4}$	18.0 ± 2.9	$16.282^{+0.598}_{-0.617}$
distance (pc)	65.03 ± 0.36	⋯	$65.390^{+0.540}_{-0.464}$
Luminosity ($L_\odot$)	$0.00711^{+0.00083}_{-0.00075}$	⋯	⋯
A_V (mag)	0 (fixed)	0 (fixed)	$\sim$0 †
F_{bol} (cgs)	⋯	$5.19(18) \times 10^{-11}$	⋯
$M_{\rm Ks}$ (mag)	7.265 ± 0.026	⋯	⋯

Note. † The resulting posterior is approximately zero and non-Gaussian as a result of using a tight uniform prior close to 0 for numerical reasons.

robust. The derived stellar parameters agreed within $1 \sim 2\sigma$, as shown in Table A1. We pick up the results from the empirical relations as our final stellar parameters in Table 1.

Appendix B
Light Contamination Analysis

Contamination leads to a decrease in the observed transit depth (the planet appears to be smaller than it truly is), and this effect is achromatic even if the host and the contaminant(s) are of different spectral types. Having simultaneous multicolor photometry allows us to measure possible light contamination from unresolved stars and consequently provides strong constraints on the false-positive scenarios discussed in Section 3.6.

Following the methods presented in Parviainen et al. (2020, 2021), we used the physics-based contamination model included in `PyTransitv21` to model the light curves using a transit model that includes a light contamination component based on model stellar spectra leveraging multicolor photometry. Fitting the transit+contamination model to MuSCAT3 light curves allows us to measure the contamination in i band,[54] the effective temperature of the host ($T_{\rm eff,H}$), and the effective temperature of the contaminant ($T_{\rm eff,C}$).

We used normal priors for the period and T_0 based on the results of our transit analysis. We also used normal priors on limb darkening, the host effective temperature, and the host star density, based on our spectroscopic analysis. Among them, the spectroscopic priors are the most important. Without a limb darkening prior, the transit fit in the g band is boxy perhaps due to the sparse data sampling. Without the $T_{\rm eff,H}$ prior, the posteriors are not well behaved. Without the host $\rho_\star$ prior, the model converges to very high values ($\sim$33g cm^{-3}), which is inconsistent with the results from our previous analyses.

The joint and marginal posteriors of the relevant parameters are shown in Figure B1. Significant levels of blending from sources with effective temperatures different from that of the host star are excluded, and also the blending from sources with $T_{\rm eff,C} \sim T_{\rm eff,H}$ is strongly constrained.

[54] We adopt i as the reference passband for simplicity.

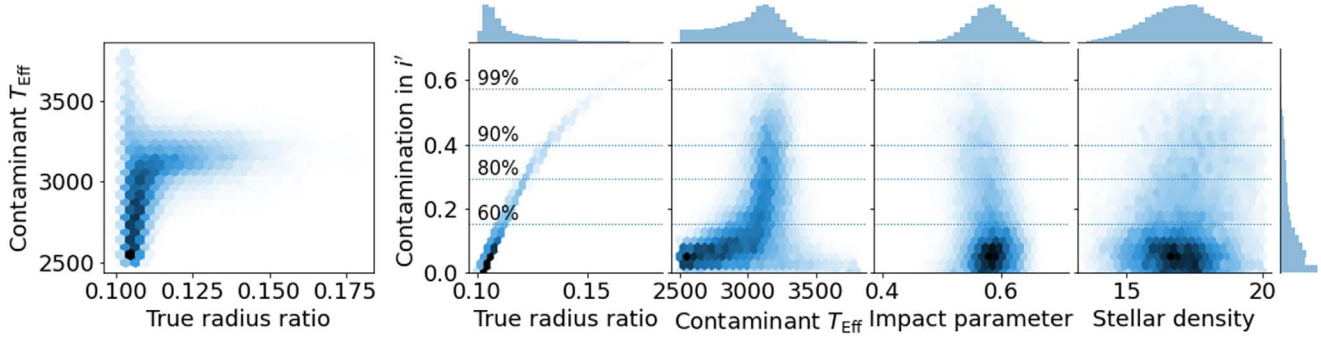

Figure B1. Joint and marginal posteriors for the key parameters from the transit+contamination modeling of the MuSCAT3 multicolor light curves. Contamination due to sources with significantly different effective temperatures than the host is ruled out.

Appendix C
HEB simulation

To assess the probability of the TOI-1696 b signal originating from an HEB, we simulate different HEB scenarios assuming that each system was composed of the primary star (TOI-1696, Star 1), plus a tertiary companion (Star 3) eclipsing a secondary companion (Star 2) every 2.5 days. For a grid of secondary and tertiary star masses ranging from 0.1 to $0.4 M_{\odot}$, we then calculated the observed maximum eclipse depth caused by Star 3 eclipsing Star 2 in the MuSCAT3 g and z bands using the following procedure. First, we interpolated $L_{\star}$ and $T_{\rm eff}$ of Star 2 and Star 3 from the Modules for Experiments in Stellar Astrophysics isochrones given their masses, and the age, metallicity, and mass of Star 1 in Table 1. We then computed the blackbody function of each star given their $T_{\rm eff}$ then convolved it with the transmission functions for each band downloaded from the SVO filter profile service.[55] We then integrated the result using the trapezoidal method and computed the bolometric flux $F_{\rm bol}$, using the integrated functions above. Using the Stefan–Boltzmann law and given $T_{\rm eff}$ and $L_{\star}$, we computed the component radii and luminosities to derive the eclipse depth.

Figure C1 shows the HEB configurations that produce eclipse depths in the g (blue) and z bands (red) that are consistent with the observed depth for two given impact parameters. The lower impact parameter corresponds to the 3σ lower limit derived from our contamination analysis while the other impact parameter corresponds to the median value derived in our transit analysis. We confirm that indeed eclipses of an HEB are always deeper in the red than in the blue bands (i.e., higher m_2/m_1 in the z band than in the g band) as the eclipsing companions are usually redder than the central star. The important point here is that the HEB configurations that produce eclipses consistent with our observation do not overlap within 1σ in the g and z bands for any reasonable impact parameters. Note also that our contamination analysis constrained possible contaminants to have the same color as the host star, so only masses very close to TOI-1696 (vertical dashed line in Figure C1) are allowed. Thus, we can rule out the HEB false-positive scenario.

[55] http://svo2.cab.inta-csic.es/theory/fps/

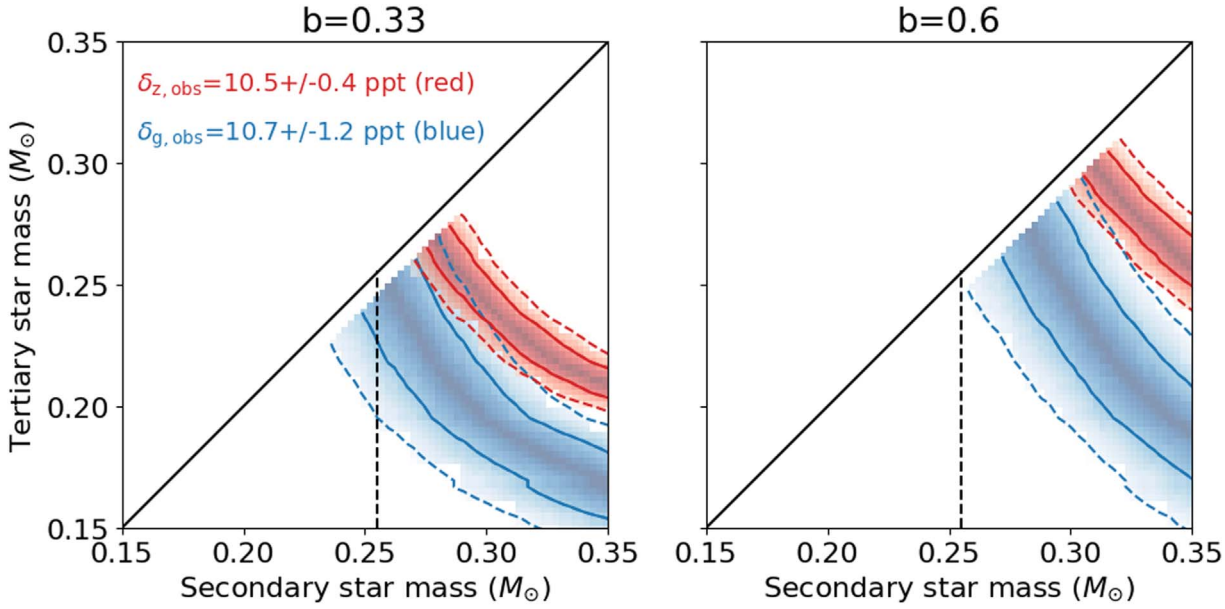

Figure C1. HEB mass configurations, which produce eclipse depths in the g band (blue) and z band (red) consistent with the observed depths (indicated in the upper left corner of the first panel). The left panel corresponds to the lower limit of the impact parameter and the right for the median value. The colored solid line and dashed lines correspond to confidence regions that are consistent with the observed depths within 1 and 2σ, respectively. The vertical black line corresponds to the mass of the central star (i.e., TOI-1696). The fact that the red and blue regions do not overlap within 1σ taking into account impact parameter rules out the HEB false-positive scenario.

Appendix D
Validation with `Vespa` and `Triceratops`

`Vespa`[56] was originally developed as a tool for the statistical validation of planet candidates identified by the Kepler mission (e.g., Morton et al. 2016), but has also been used extensively to validate planets from subsequent missions, such as K2 (e.g., Livingston et al. 2018; de Leon et al. 2021). `Vespa` compares the likelihood of a planetary scenario to the likelihoods of several astrophysical false-positive scenarios involving eclipsing binaries (EBs), hierarchical triple systems (HEBs), background eclipsing binaries (BEBs), and the double-period cases of all these scenarios. The likelihoods and priors for each scenario are based on the shape of the transit signal, the star's location in the Galaxy, and single-, binary-, and triple-star model fits to the observed photometric and spectroscopic properties of the star generated using `isochrones`. We used the MuSCAT3 light curve because of its high S/N and low levels of limb darkening, which provides the best constraint on the transit shape. We also used the Gemini and Palomar contrast curves described in Section 2.6, a maximum aperture radius of `maxrad` $= 3''$ (interior to which the transit signal must be produced), and ran the simulation using a population size of $n = 10^6$, resulting to a formal FPP $< 1 \times 10^{-6}$. This value is much lower than the commonly used FPP $< 1\%$ criteria for planet validation (e.g., Morton et al. 2016).

We also used `Triceratops`[57], which is a tool developed to validate TOIs (Giacalone & Dressing 2021; Giacalone et al. 2021) by calculating the Bayesian probabilities of the observed transit originating from several scenarios involving the target star, nearby resolved stars, and hypothetical unresolved stars in the immediate vicinity of the target. These probabilities were then compared to calculate a false-positive probability (the total probability of the transit originating from something other than a planet around the target star) and a nearby false-positive probability (NFPP; the total probability of the transit originating from a nearby resolved star). Given our follow-up photometry rules out nearby stars as a potential source of the transit signal, we eliminate all stars except the target in the `Triceratops`analysis. As an additional constraint, we use the contrast curve from our follow-up speckle imaging as a direct input in `Triceratops`. For the sake of reliability, we performed the calculation 20 times for the planet candidate and found FPP $= 2 \times 10^{-3}$. Giacalone et al. (2021) noted that TOIs with FPP $< 1.5 \times 10^{-2}$ have a high enough probability of being bona fide planets to be considered validated. Thus, the low FPPs calculated using `Vespa` and `Triceratops` provide further evidence to statistically validate TOI-1696.01 as a planet.

[56] https://github.com/timothydmorton/VESPA
[57] https://github.com/stevengiacalone/triceratops

ORCID iDs

Mayuko Mori https://orcid.org/0000-0002-5609-4427
John H. Livingston https://orcid.org/0000-0002-4881-3620
Norio Narita https://orcid.org/0000-0001-8511-2981
Teruyuki Hirano https://orcid.org/0000-0003-3618-7535
Akihiko Fukui https://orcid.org/0000-0002-4909-5763
Karen A. Collins https://orcid.org/0000-0001-6588-9574
Naho Fujita https://orcid.org/0000-0002-5791-970X
Yasunori Hori https://orcid.org/0000-0003-4676-0251
Hiroyuki Tako Ishikawa https://orcid.org/0000-0001-6309-4380
Keivan G. Stassun https://orcid.org/0000-0002-3481-9052
Noriharu Watanabe https://orcid.org/0000-0002-7522-8195
Steven Giacalone https://orcid.org/0000-0002-8965-3969
Courtney D. Dressing https://orcid.org/0000-0001-8189-0233
Allyson Bieryla https://orcid.org/0000-0001-6637-5401
Eric L. N. Jensen https://orcid.org/0000-0002-4625-7333
Bob Massey https://orcid.org/0000-0001-8879-7138
Avi Shporer https://orcid.org/0000-0002-1836-3120

Masayuki Kuzuhara https://orcid.org/0000-0002-4677-9182
David Charbonneau https://orcid.org/0000-0002-9003-484X
David R. Ciardi https://orcid.org/0000-0002-5741-3047
John P. Doty https://orcid.org/0000-0003-2996-8421
Emma Esparza-Borges https://orcid.org/0000-0002-2341-3233
Hiroki Harakawa https://orcid.org/0000-0002-6197-5544
Klaus Hodapp https://orcid.org/0000-0003-0786-2140
Masahiro Ikoma https://orcid.org/0000-0002-5658-5971
Kai Ikuta https://orcid.org/0000-0002-5978-057X
Jon M. Jenkins https://orcid.org/0000-0002-4715-9460
Takanori Kodama https://orcid.org/0000-0001-9032-5826
Vigneshwaran Krishnamurthy https://orcid.org/0000-0003-2310-9415
Tomoyuki Kudo https://orcid.org/0000-0002-9294-1793
Nobuhiko Kusakabe https://orcid.org/0000-0001-9194-1268
David W. Latham https://orcid.org/0000-0001-9911-7388
Brian McLean https://orcid.org/0000-0002-8058-643X
Felipe Murgas https://orcid.org/0000-0001-9087-1245
Jun Nishikawa https://orcid.org/0000-0001-9326-8134
Taku Nishiumi https://orcid.org/0000-0003-1510-8981
Masashi Omiya https://orcid.org/0000-0002-5051-6027
Hugh P. Osborn https://orcid.org/0000-0002-4047-4724
Enric Palle https://orcid.org/0000-0003-0987-1593
Hannu Parviainen https://orcid.org/0000-0001-5519-1391
George R. Ricker https://orcid.org/0000-0003-2058-6662
Sara Seager https://orcid.org/0000-0002-6892-6948
Huan-Yu Teng https://orcid.org/0000-0003-3860-6297
Yuka Terada https://orcid.org/0000-0003-2887-6381
Joseph D. Twicken https://orcid.org/0000-0002-6778-7552
Roland Vanderspek https://orcid.org/0000-0001-6763-6562
Sébastien Vievard https://orcid.org/0000-0003-4018-2569
Joshua N. Winn https://orcid.org/0000-0002-4265-047X
Yujie Zou https://orcid.org/0000-0002-5609-4427
Motohide Tamura https://orcid.org/0000-0002-6510-0681

References

Anderson, O. L., Dubrovinsky, L., Saxena, S. K., & LeBihan, T. 2001, GeoRL, 28, 399
Astropy Collaboration, Price-Whelan, A. M., Sipőcz, B. M., et al. 2018, AJ, 156, 123
Astropy Collaboration, Robitaille, T. P., Tollerud, E. J., et al. 2013, A&A, 558, A33
Bellm, E. C., Kulkarni, S. R., Graham, M. J., et al. 2019, PASP, 131, 018002
Belokurov, V., Penoyre, Z., Oh, S., et al. 2020, MNRAS, 496, 1922
Borucki, W. J., Koch, D., Basri, G., et al. 2010, Sci, 327, 977
Bouma, L. G., Hartman, J. D., Brahm, R., et al. 2020, AJ, 160, 239
Brande, J., Crossfield, I. J. M., Kreidberg, L., et al. 2022, arXiv:2201.04197
Brown, T. M., Baliber, N., Bianco, F. B., et al. 2013, PASP, 125, 1031
Burrows, A., Heng, K., & Nampaisarn, T. 2011, ApJ, 736, 47
Castro González, A., Díez Alonso, E., Menéndez Blanco, J., et al. 2020, MNRAS, 499, 5416
Charbonneau, D., Berta, Z. K., Irwin, J., et al. 2009, Natur, 462, 891
Claret, A. 2017, A&A, 600, A30
Claret, A., Hauschildt, P. H., & Witte, S. 2012, A&A, 546, A14
Cointepas, M., Almenara, J. M., Bonfils, X., et al. 2021, A&A, 650, A145
Collins, K. A., Kielkopf, J. F., Stassun, K. G., & Hessman, F. V. 2017, AJ, 153, 77
Cushing, M. C., Vacca, W. D., & Rayner, J. T. 2004, PASP, 116, 362
Cutri, R. M., Wright, E. L., Conrow, T., et al. 2021, yCat, II/328
de Leon, J. P., Livingston, J., Endl, M., et al. 2021, MNRAS, 508, 195
Dressing, C. D., Hardegree-Ullman, K., Schlieder, J. E., et al. 2019, AJ, 158, 87
Erkaev, N. V., Kulikov, Y. N., Lammer, H., et al. 2007, A&A, 472, 329
ExoFOP 2019, Exoplanet Follow-up Observing Program - TESS
Foreman-Mackey, D. 2018, RNAAS, 2, 31
Foreman-Mackey, D., Agol, E., Ambikasaran, S., & Angus, R. 2017, AJ, 154, 220
Foreman-Mackey, D., Barentsen, G., & Barclay, T. 2019, dfm/exoplanet: exoplanet v0.1.5, Zenodo, doi:10.5281/zenodo.2587222
Fukui, A., Narita, N., Tristram, P. J., et al. 2011, PASJ, 63, 287
Gagné, J., Mamajek, E. E., Malo, L., et al. 2018, ApJ, 856, 23
Gelman, A., & Rubin, D. B. 1992, StaSc, 7, 457
Giacalone, S., & Dressing, C. D. 2021, AJ, 161, 24
Giacalone, S., Dressing, C. D., Jensen, E. L. N., et al. 2021, AJ, 161, 24
Girardi, L., Groenewegen, M. A. T., Hatziminaoglou, E., & da Costa, L. 2005, A&A, 436, 895
Guerrero, N. M., Seager, S., Huang, C. X., et al. 2021, ApJS, 254, 39
Hauschildt, P. H., Allard, F., & Baron, E. 1999, ApJ, 512, 377
Hayward, T. L., Brandl, B., Pirger, B., et al. 2001, PASP, 113, 105
Hippke, M., & Heller, R. 2019, A&A, 623, A39
Hirano, T., Kuzuhara, M., Kotani, T., et al. 2020, PASJ, 72, 93
Hirano, T., Livingston, J. H., Fukui, A., et al. 2021, AJ, 162, 161
Hoffman, M. D., & Gelman, A. 2014, J. Mach. Learn. Res., 15, 1593
Howell, S. B., Everett, M. E., Sherry, W., Horch, E., & Ciardi, D. R. 2011, AJ, 142, 19
Ionov, D. E., & Shematovich, V. I. 2015, SoSyR, 49, 339
Ishikawa, H. T., Aoki, W., Kotani, T., et al. 2020, PASJ, 72, 102
Ishikawa, H. T., Aoki, W., Hirano, T., et al. 2022, AJ, 163, 72
Jackson, A. P., Davis, T. A., & Wheatley, P. J. 2012, MNRAS, 422, 2024
Jenkins, J. M. 2002, ApJ, 575, 493
Jenkins, J. M., Chandrasekaran, H., McCauliff, S. D., et al. 2010, Proc. SPIE, 7740, 77400D
Jenkins, J. M., Twicken, J. D., McCaulif, S., et al. 2016, Proc. SPIE, 9913, 99133E
Jenkins, J. S., Díaz, M. R., Kurtovic, N. T., et al. 2020, NatAs, 4, 1148
Kanodia, S., Wolfgang, A., Stefansson, G. K., Ning, B., & Mahadevan, S. 2019, ApJ, 882, 38
Karki, B. B., Wentzcovitch, R. M., de Gironcoli, S., & Baroni, S. 2000, PhRvB, 62, 14750
Kempton, E. M. R., Bean, J. L., Louie, D. R., et al. 2018, PASP, 130, 114401
Kochanek, C. S., Shappee, B. J., Stanek, K. Z., et al. 2017, PASP, 129, 104502
Kotani, T., Tamura, M., Nishikawa, J., et al. 2018, Proc. SPIE, 10702, 1070211
Kuzuhara, M., Hirano, T., Kotani, T., et al. 2018, Proc. SPIE, 10702, 1070260
Li, J., Tenenbaum, P., Twicken, J. D., et al. 2019, PASP, 131, 024506
Livingston, J. H., Crossfield, I. J. M., Petigura, E. A., et al. 2018, AJ, 156, 277
Lopez, E. D. 2017, MNRAS, 472, 245
Luger, R., Agol, E., Foreman-Mackey, D., et al. 2019, AJ, 157, 64
Mann, A. W., Brewer, J. M., Gaidos, E., Lépine, S., & Hilton, E. J. 2013, AJ, 145, 52
Mann, A. W., Dupuy, T., Kraus, A. L., et al. 2019, ApJ, 871, 63
Mann, A. W., Feiden, G. A., Gaidos, E., Boyajian, T., & von Braun, K. 2015, ApJ, 804, 64
Mann, A. W., Gaidos, E., Mace, G. N., et al. 2016, ApJ, 818, 46
Masci, F. J., Laher, R. R., Rusholme, B., et al. 2019, PASP, 131, 018003
Mazeh, T., Holczer, T., & Faigler, S. 2016, A&A, 589, A75
McCully, C., Volgenau, N. H., Harbeck, D.-R., et al. 2018, Proc. SPIE, 10707, 107070K
Morton, T. D. 2015a, VESPA: False positive probabilities calculator, Astrophysics Source Code Library, ascl:1503.011
Morton, T. D. 2015b, isochrones: Stellar model grid package, Astrophysics Source Code Library, ascl:1503.010
Morton, T. D., Bryson, S. T., Coughlin, J. L., et al. 2016, ApJ, 822, 86
Muiños, J. L., & Evans, D. W. 2014, AN, 335, 367
Murgas, F., Astudillo-Defru, N., Bonfils, X., et al. 2021, A&A, 653, A60
Narita, N., Fukui, A., Kusakabe, N., et al. 2015, JATIS, 1, 045001
Narita, N., Fukui, A., Yamamuro, T., et al. 2020, Proc. SPIE, 11447, 114475K
NASA Exoplanet Science Institute 2020, Planetary Systems Table
Newton, E. R., Charbonneau, D., Irwin, J., et al. 2014, AJ, 147, 20
Newton, E. R., Charbonneau, D., Irwin, J., et al. 2022, tellrv: Radial velocities for low-resolution NIR spectra, Astrophysics Source Code Library, ascl:2201.007
Nocedal, J., & Wright, S. J. 2006, Numerical Optimization (2nd edn; New York: Springer)
Owen, J. E., & Wu, Y. 2017, ApJ, 847, 29
Parviainen, H. 2015, MNRAS, 450, 3233
Parviainen, H., Palle, E., Zapatero-Osorio, M. R., et al. 2020, A&A, 633, A28
Parviainen, H., Palle, E., Zapatero-Osorio, M. R., et al. 2021, A&A, 645, A16
Pecaut, M. J., & Mamajek, E. E. 2013, ApJS, 208, 9

Rasmussen, C. E., & Williams, C. K. I. 2005, Gaussian Processes for Machine Learning (Adaptive Computation and Machine Learning) (Cambridge, MA: MIT Press)
Rayner, J. T., Toomey, D. W., Onaka, P. M., et al. 2003, PASP, 115, 362
Reid, I. N., Brewer, C., Brucato, R. J., et al. 1991, PASP, 103, 661
Ricker, G. R., Winn, J. N., Vanderspek, R., et al. 2015, JATIS, 1, 014003
Rogers, L. A. 2015, ApJ, 801, 41
Salpeter, E. E., & Zapolsky, H. S. 1967, PhRv, 158, 876
Salvatier, J., Wiecki, T. V., & Fonnesbeck, C. 2016, PeerJ Comp. Sci., 2, e55
Saumon, D., Chabrier, G., & van Horn, H. M. 1995, ApJS, 99, 713
Scott, N. J. 2019, BAAS, 51, 6
Seager, S., Kuchner, M., Hier-Majumder, C. A., & Militzer, B. 2007, ApJ, 669, 1279
Shematovich, V. I., Ionov, D. E., & Lammer, H. 2014, A&A, 571, A94
Skrutskie, M. F., Cutri, R. M., Stiening, R., et al. 2006, AJ, 131, 1163
Smith, J. C., Stumpe, M. C., Van Cleve, J. E., et al. 2012, PASP, 124, 1000
Stassun, K. G., Collins, K. A., & Gaudi, B. S. 2017, AJ, 153, 136
Stassun, K. G., & Torres, G. 2016, AJ, 152, 180
Stassun, K. G., & Torres, G. 2021, ApJL, 907, L33
Stassun, K. G., Oelkers, R. J., Pepper, J., et al. 2018, AJ, 156, 102
Stumpe, M. C., Smith, J. C., Catanzarite, J. H., et al. 2014, PASP, 126, 100
Stumpe, M. C., Smith, J. C., Van Cleve, J. E., et al. 2012, PASP, 124, 985
Szabó, G. M., & Kiss, L. L. 2011, ApJL, 727, L44
Tamura, M., Suto, H., Nishikawa, J., et al. 2012, Proc. SPIE, 8446, 84461T
Tody, D. 1993, in ASP Conf. Ser., 52, Astronomical Data Analysis Software and Systems II, ed. R. J. Hanisch, R. J. V. Brissenden, & J. Barnes (San Francisco, CA: ASP), 173
Toledo-Padrón, B., González Hernández, J. I., Rodríguez-López, C., et al. 2019, MNRAS, 488, 5145
Twicken, J. D., Catanzarite, J. H., Clarke, B. D., et al. 2018, PASP, 130, 064502
Vacca, W. D., Cushing, M. C., & Rayner, J. T. 2003, PASP, 115, 389
Watson, A. J., Donahue, T. M., & Walker, J. C. G. 1981, Icar, 48, 150
Weiss, L. M., & Marcy, G. W. 2014, ApJL, 783, L6
Wells, R. D., Rackham, B. V., Schanche, N., et al. 2021, A&A, 653, A97
West, R. G., Gillen, E., Bayliss, D., et al. 2019, MNRAS, 486, 5094
Zeng, L., & Sasselov, D. 2013, PASP, 125, 227